Time-of-day effects of drugs revealed by high-throughput deep phenotyping

Running title: Time-of-day effects of drugs

Authors: Carolin Ector[1,2], Christoph Schmal[3], Jeff Didier[4], Sébastien De Landtsheer[4], Anna-Marie Finger[5,6], Francesca Müller-Marquardt[1,7], Johannes Schulte[8,9], Thomas Sauter[4], Ulrich Keilholz[1,10], Hanspeter Herzel[3,11], Achim Kramer[5], Adrián E. Granada*[1,10]

First author: Carolin Ector || **Corresponding author:** adrian.granada@charite.de

Affiliations:

1. Charité Comprehensive Cancer Center, Charité – Universitätsmedizin Berlin, Charitéplatz 1, 10117 Berlin, Germany.
2. Faculty of Life Sciences, Humboldt-Universität zu Berlin, Invalidenstraße 42, 10115 Berlin, Germany.
3. Institute for Theoretical Biology, Humboldt-Universität zu Berlin, Philippstraße 13, 10115 Berlin, Germany.
4. Department of Life Sciences and Medicine, University of Luxembourg, 2, Avenue de l'Université, L-4365 Esch-sur-Alzette, Luxembourg.
5. Institute for Medical Immunology, Charité – Universitätsmedizin Berlin, Charitéplatz 1, 10117 Berlin, Germany.
6. Present address: Department of Anatomy, University of California, San Francisco, 513 Parnassus Avenue HSW 1330, San Francisco, CA 94143-0452, USA.
7. Present address: Institute of Research for Development, University of Montpellier, 911 Av. Agropolis, 34394 Montpellier, France.
8. Department of Pediatric Oncology, Hematology and Stem Cell Transplantation, Charité – Universitätsmedizin Berlin, Charitéplatz 1, 10117 Berlin, Germany.
9. Present address: Clinic for Pediatrics and Adolescent Medicine, Universitätsklinikum Tübingen, Hoppe-Seyler-Str. 1, 72076 Tübingen, Germany.
10. German Cancer Consortium (DKTK), Berlin, Germany.
11. Charité – Universitätsmedizin Berlin, Charitéplatz 1, 10117 Berlin, Germany.

Author contributions:

C.E., A.K., and A.E.G. conceived and planned the experiments.
C.E. performed the experiments. F.M.M. performed bioluminescence recordings of three cell lines.
C.E., C.S., J.D., and S.D.L. analyzed the data.
A.M.F. and A.K. supported in the planning and implementation of the bioluminescence recordings.
C.E., C.S., A.M.F., J.D., S.D.L., J.S., T.S., U.K, H.H., A.K., and A.E.G. contributed to the interpretation of the results.
C.E. and A.E.G wrote the manuscript. All authors provided critical feedback and helped shape the research and manuscript.

Keywords: circadian clock, drug sensitivity, systems biology, chronopharmacology.

Abbreviations:

5-FU, 5-fluorouracil; AC, autocorrelation; ATCC, American type culture collection; BL1, basal-like1; BL2, basal-like2; BMAL1, brain and muscle arnt-like protein-1; CI, confidence interval; CLOCK, circadian locomotor output cycles protein kaput; CRY, cryptochrome; CWT, continuous wavelet transform; dKO, double-knockout; DMEM, Dulbecco's Modified Eagle Medium; DMSO, dimethyl sulfoxide; DWT, discrete wavelet transform; EGF, epidermal growth factor; GR, growth rate inhibition; LDA, linear discriminant analysis; Luc, luciferase; MES, mesenchymal; mTOR, mammalian target of rapamycin; NLS, nuclear localization sequence; PARP, poly ADP ribose polymerase; PCA, principal component analysis; PER2, period2; PI3K, phosphatidylinositol 3-kinase/alpha serine/ threonine-protein kinase; ROR, RAR-related orphan receptor; RPMI, Roswell Park Memorial Institute medium; SCN, suprachiasmatic nucleus; sKO, single-knockout; TNBC, triple-negative breast cancer; ToD, time-of-day; TPM, transcripts per million.

Abstract

The circadian clock, a fundamental biological regulator, governs essential cellular processes in health and disease. Circadian-based therapeutic strategies are increasingly gaining recognition as promising avenues. Aligning drug administration with the circadian rhythm can enhance treatment efficacy and minimize side effects. Yet, uncovering the optimal treatment timings remains challenging, limiting their widespread adoption. In this work, we introduce a novel high-throughput approach integrating live-imaging and data analysis techniques to deep-phenotype cell models, evaluating their circadian rhythms, growth, and drug responses. We devised a streamlined process for profiling drug sensitivities across different times of the day, identifying optimal treatment windows and responsive cell types and drug combinations.

Finally, we implement multiple computational tools to uncover cellular and genetic factors shaping time-of-day drug sensitivity. Our versatile approach is adaptable to various biological models, facilitating its broad application and relevance. Ultimately, this research leverages circadian rhythms to optimize drug treatments, promising improved outcomes and transformative treatment strategies.

Introduction

The circadian clock is a central regulator of multiple physiological and behavioral processes found in cyanobacteria, plants, fungi, and animals. In mammals, the hierarchical organization of the circadian system ensures coordinated biological rhythms from the level of the individual cell to whole organism level[1]. Primate and mouse studies showed that up to 40% of all protein-coding genes are rhythmically expressed in a tissue-specific manner[2,3]. These clock-controlled genes regulate key biological processes such as metabolism[4,5], cell proliferation[6], immune response[7], DNA repair and apoptosis[8].

Disruption of the circadian system is classified as a carcinogen and is associated with multiple cancer subtypes[9-12]. Cancer hallmarks such as sustained proliferation and metastasis[13,14] have been linked to the circadian clock[15,16] and patients with mutations in circadian clock genes exhibit lower survival rates[17-19]. Beyond its role in cancer development, the circadian clock directly interacts with therapeutic targets that affect drug responses[19-21]. Consistent with these observations, recent works have shown that administration of chemotherapeutic agents aligned with the circadian rhythm change their degree of efficacy throughout the day[20,22-24]. Despite the broad recognition of the benefits of circadian-based drug treatments[22,25,26], an efficient strategy to identify optimal treatment times remains elusive, creating a bottleneck in the implementation. In addition, the mechanisms shaping time-of-day (ToD) sensitivity profiles remain widely unknown.

Here, we introduce a novel method for the thorough characterization of time-of-day responses in tumor and healthy tissue cell models (**Fig.1**). Using an array of experimental and data analysis methods we perform a deep-phenotyping of the critical cellular factors underlying time-of-day responses, i.e., the circadian clock strength, growth dynamics and drug response features. We then deploy a new high-throughput strategy to obtain ToD profiles in a panel of drugs and cell line models. Comparing tumor versus non-tumor ToD profiles provides candidate treatment timings to increase efficacy and reduce toxicity. We subsequently integrate our dataset with publicly available gene-expression databases to rigorously address three fundamental questions in the field of circadian pharmacology, known as chronopharmacology. These questions are: (A) what is the optimal time-of-day for drug treatment? (B) which cell subtype benefits the most from a circadian-aligned drug treatment? and (C) how do cellular features shape time-of-day profiles? Finally, we define a chronotherapeutic index, ranking

cellular models and drug agents that stands to gain the most benefit from circadian-based treatments.

Results

Deep circadian phenotyping in cancer cell models

Despite the increasing recognition of the circadian clock in cancer, the extent to which different cancer subtypes maintain circadian rhythmicity remains poorly understood. To address this, we integrate recordings of circadian clock activity with comprehensive time-series analysis techniques, as depicted in **Fig. 2a**. To robustly characterize the circadian clock network, we monitored the positive and negative feedback arms of the molecular clock using a combination of two circadian luciferase reporters for *Bmal1* and *Per2* (**Fig. 2b**). In **Fig. 2c** we show representative raw luciferase signals from the breast cancer cell line MDAMB468, and the corresponding detrended and normalized signals[27]. As expected for a robust functional clock network, *Bmal1* and *Per2* signals show stable anti-phasic expression patterns throughout the recording (**Fig. 2c** and **Supplementary Fig. 1a,b)**.

Circadian clock strength varies in cancer and healthy tissue models

Following the acquisition of *Bmal1* and *Per2* expression dynamics, we conducted a comprehensive circadian phenotyping of the signals. For this we implemented a strategy that integrates three complementary time-series analysis techniques, i.e., autocorrelation (AC), continuous wavelet transform (CWT), and multiresolution analysis (MRA). Using this approach we screened a broad panel of cell models, including non-malignant breast epithelial MCF10A, cancer cell models of various entities (breast cancer, neuroblastoma, and sarcoma) as well as two knockout variants of osteosarcoma U-2 OS cells with a single deletion in the circadian clock gene *Cry1* (U-2 OS sKO) or paired with a deletion in the *Cry2* locus[28] (U-2 OS dKO). Calculating the autocorrelation function from each recording provides the strength and period values, obtained from the second peak ordinate and abscissa (lag), respectively (**Fig. 2d**). This analysis showed a wide range of circadian strengths across models with the U-2 OS wild-type ranking highest with a median autocorrelation value of 0.74, whereas U-2 OS sKO and U-2 OS dKO variants ranked lowest with median correlation values of -0.04 (p=3.5×10^{-10})

124 and 0.09 (p=1.3×10^{-10}), respectively (**Fig. 2e**). Heterogeneity between and within cancer
125 entities was further observed for the oscillation period ranging from short periods of ~21 h in
126 HCC1806 and U-2 OS sKO cells (p=2.1×10^{-3}) to longer periods of ~26 h in MDAMB468 and
127 MCF10A cells. U-2 OS dKO (34.8 h, p=2.6×10^{-4}) and the neuroblastoma cell line SH-SY5Y
128 (39.2 h) showed periods well above the circadian range and were excluded from this analysis
129 (**Fig. 2f**). Consistent with these results, detrended signal traces of the different cell models and
130 additional breast cancer cell lines indicate high variability in circadian clock signals across the
131 models tested (**Supplementary Fig. 1c**).
132 To capture the non-stationary aspects of circadian signals, we employed continuous wavelet
133 transform, a prevalent technique for analyzing dynamic temporal signals[29]. **Fig. 2g** shows a
134 CWT power spectrum heatmap of *Bmal1* signal from the MDAMB468 example. The heatmap
135 displays signal components (0–40 h period) over the 120-h recording, color-coded by relative
136 power (see **Methods**). The most important high-power component is marked by a persistent
137 ridge for each time point. Strong signals exhibit continuous long ridges whereas weaker signals
138 have short and discontinuous ridges. As a complementary measure of clock strength, we
139 quantified the ridge length from all our recordings. Our analysis shows that U-2 OS cells have
140 a well-maintained clock with a median ridge length of 4.1 days, closely followed by MCF7,
141 MDAMB468 and MCF10A cells (3.4–3.8 days). U-2 OS sKO and dKO cells showed ridges
142 shorter than two days (1.9 days [p=6.7×10^{-4}] and 1.5 days [p=5.5×10^{-5}], respectively) (**Fig.
143 2h**).
144 For a more comprehensive understanding of the signal components, we next implemented
145 multiresolution analysis. MRA involves decomposing the detrended signal into four distinct
146 component bands, namely the noise (1–4 h), ultradian (4–16 h), circadian (16–32 h) and
147 infradian (32–48 h) components (see **Methods**). In **Fig. 2i** we present an example of
148 MDAMB468 *Bmal1*-Luc where 75.9% of the signal is in the circadian range, 4.7% in the noise
149 and the remaining 19.4% in the ultradian or infradian range. To obtain an analogous signal-to-
150 noise measure of all recorded cell models, we plotted the circadian component
151 ("circadianicity") versus the noise component and observed a broad range of ratios (**Fig. 2j**).
152 Consistent with our previous analysis, U-2 OS cells show strong circadian signal with the
153 lowest noise levels (<1%) and the highest proportion of circadian components (~93%) for both
154 reporters. Knockout of *Cry1* or *Cry1/Cry2* reduced the circadian component to 59%
155 (p=1×10^{-6}) and 40% (p=5.6×10^{-7}), respectively, while increasing the noise component by 5.8-

156 fold in the single knockout and by 209-fold in the double knockout. This signal-to-noise
157 analysis map indicates that signals from the *Per2*-reporter were slightly more circadian and
158 less noisy than those from the *Bmal1*-reporter (**Fig. 2j** and **Supplementary Fig. 1d**). Finally,
159 to obtain a global strength metric, we normalized each circadian parameter to its respective
160 maximum value across all tested cell line models and computed the mean, facilitating a gradual
161 ranking of cell models from low to high circadian strength (**Fig. 2k**, see **Methods**).
162 In summary, we identified heterogeneous circadian clock phenotypes in the different models
163 tested, suggesting a strong clock in U-2 OS, MCF7, MDAMB468 and MCF10A cells and an
164 impaired but present clock in GIMEN and HCC1806 cells. These results challenge the common
165 expectation that most cancer cells have a weak clock and underscore the significance of
166 defining gradual metrics of circadian strength in a model-specific manner.
167

168 Growth and drug response dynamics in cancer cell models

169 Together with circadian potency, cell growth dynamics and how cells respond to drug treatment
170 in time is expected to influence responses along the day. Thus, we next evaluated growth
171 characteristics and drug sensitivities across a spectrum of drug and cell line models. To
172 showcase our approach's ability in detecting within-tissue differences, we examined nine cell
173 lines of the triple-negative breast cancer (TNBC) subtype alongside the non-malignant
174 MCF10A breast cell model. To capture the dynamics of growth and drug response, we
175 implemented a live-cell imaging setup using two imaging channels, the brightfield for
176 confluency and the fluorescence channel for nuclear detection (**Fig. 3a**). **Fig. 3b** shows
177 representative snapshots of both imaging channels from MDAMB468 cells under unperturbed
178 conditions. Frame-by-frame quantification provides growth trajectories for each cell model
179 tested (**Supplementary Fig. 2a)**, with MDAMB468 cells showing a 5.3-fold increase in growth
180 and reaching approximately 100% confluency after 4 days (**Fig. 3c**). Quantification of doubling
181 times (DTs) calculated from confluency and cell numbers correlated well across the 10 cell line
182 models tested (R^2=0.69) (**Supplementary Fig. 2b**). Upon examining the normalized cell
183 number trajectories, we observed substantial variability in growth across the cell line models,
184 ranging from approximately 2- to 16-fold over the 4-day recordings (**Fig. 3d**). To capture
185 growth signatures from the entire recording, we fitted an exponential function to each time
186 series and obtained the growth rate k for each trajectory (**Fig. 3e**). As expected, cell number

187 growth rates and doubling times exhibit a strong anticorrelation (R^2=0.83) (**Fig. 3f** and
188 **Supplementary Fig. 2c**).
189 Next, we studied the response of the cancer cell models upon treatment with a panel of seven
190 drugs targeting a broad range of mechanisms and pathways, i.e., the DNA synthesis inhibitors
191 5-FU and doxorubicin, mitosis-inhibiting alisertib and paclitaxel, the PI3K/AKT/mTOR
192 inhibitor torin2, as well as cisplatin and olaparib which target the DNA damage response
193 (DDR) pathway (**Fig. 3g**). We then tracked responses to a broad range of drug concentrations,
194 as exemplified in **Fig. 3h** by MDAMB468's olaparib treatment. Here, doses up to 1.5 µM
195 resulted in slightly slower growth relative to the control, while 6.3 µM of olaparib significantly
196 hindered growth, and ≥25 µM led to total inhibition and cell death. Fitting an exponential
197 function to growth curves yielded positive growth rate values for weak doses while higher
198 doses resulted in negative growth rates, indicating population decline. Using this approach, we
199 next quantified the response and stratified all tested cell lines and drugs.
200

201 Multi-parametric evaluation of drug sensitivity reveals heterogeneity 202 between and within models

203 Accurate assessment of drug effects is essential for identifying exploitable weaknesses in
204 cancer treatments. To obtain robust drug sensitivity metrics, we employed the normalized
205 growth rate inhibition (*GR*) curve approach as described by Hafner *et al.*[30]. Here, *GR* values
206 are calculated as the ratio between growth rates under treated and untreated conditions and
207 normalized to a single cell division. Fitting a dose-response equation to *GR* values yields five
208 drug sensitivity parameters, namely, the concentrations at half-maximal effect (GEC_{50}) and at
209 which GR=0.5 (GR_{50}), the drug effect at infinite concentration (GR_{inf}), the Hill coefficient of
210 the sigmoidal fit (*Hill coeff.*), and the area over the curve (GR_{AOC}) (**Fig. 3i**). Interestingly, when
211 the same cell line was treated with different cancer drugs at their respective concentration
212 evoking a saturating GR_{inf} response distinct drug-dependent trajectories emerged (**Fig. 3j**). This
213 underscores the importance of a time-resolved approach for characterizing drug sensitivity
214 across different drugs and, accordingly, across distinct cell line models.
215 We next compared a subset of drug-sensitivity metrics and cell line models for the different
216 drugs tested (**Fig. 3k–m**). While most drugs were able to induce death in the subset of cell lines
217 to varying degrees, we identified three drugs that resulted in partial growth inhibition of

218 HCC1806, namely olaparib, 5-FU and alisertib (**Fig. 3k**). Hierarchical clustering of GR_{inf}
219 values revealed a grouping of the two TNBC cell lines and while this clustering was maintained
220 for the GEC_{50} values (**Fig. 3l**), the Hill coefficient resulted in a different clustering of the cell
221 lines (**Fig. 3m**). To explore the potential relationships between various sensitivity metrics, we
222 combined data from multiple drugs and cell models and computed cross-correlations, revealing
223 significant associations among GEC_{50}, GR_{50}, and EC_{50} values ($p \leq 0.0001$) (**Fig. 3n**).
224 Additionally, significant yet less pronounced correlations emerged between the Hill coefficient
225 and different drug sensitivity parameters, whereas the GR_{inf} and GR_{AOC} values showed minimal
226 correlation with other metrics. For complete *GR* curves and information on additionally tested
227 cell lines and drugs, see **Supplementary Fig. 3** and **Supplementary Table 1**.
228

229 ## Variability throughout the day depends on the drug and tissue model

230 The presence of a robust circadian clock combined with drugs that efficiently affect growth in
231 a tumor model are promising prerequisites for identifying drug variability throughout the day.
232 However, these prerequisites do not provide a priori insights into the specific time-of-day
233 response profile. To systematically screen ToD drug sensitivities, we developed a new
234 experimental strategy designed to significantly reduce the investigator's workload and number
235 of consecutive drug perturbations, thereby increasing throughputness, reproducibility and
236 accuracy (**Fig. 4a**). In this new approach, cell populations are seeded 24 h prior to the start of
237 continuous live-cell imaging followed by performing a 3-step circadian clock resetting protocol
238 in which separate cell populations receive a dexamethasone pulse at three different times (0, 4,
239 8 h). To test cells in later stages of the circadian cycle, drugs are administered at their estimated
240 half effective dose 32 and 48 h after the first resetting step, creating a range of time differences
241 between reset and treatment of 0, 4, 8, 16, 20 and 24 h in relative circadian time (**Fig. 4a**, *right*
242 *panel*). The effects of the different treatment times on cell growth were monitored by live-cell
243 imaging up to day 6, enabling the evaluation of drug responses for 4 days in both treatment
244 groups, as shown for the alisertib-treated TNBC cell line HCC1937 in **Fig. 4b**. In typical ToD
245 assays, cells are constantly proliferating during the 24 hours of ToD treatments, resulting in
246 varying cellular densities at the time of the drug treatments. These varying cell densities have
247 the potential to influence drug responses in vitro, possibly concealing or introducing bias when
248 determining ToD-specific drug effects. To account for different cell densities at the time of

249 treatment, drug responses are determined as the ratio of the number of cells at the time of each
250 treatment to the number of cells 96 h after each treatment, keeping the time-window from
251 treatment to evaluation identical across conditions (**Fig. 4c**, *left panel*). To highlight relative
252 response differences within a day, results are presented relative to the circadian time of 0 h.
253 Values >1 indicate increased resistance, while values <1 indicate higher sensitivity compared
254 to treatment at time 0 h (**Fig. 4c**, *right panel*). We quantify the maximum variability in relative
255 responses as the ToD Maximum Range (ToD_{MR}).
256 Our next objective was to explore the variability of ToD profiles of different drugs within a
257 subset of TNBC cells. To accomplish this, we screened ten cell line models shown in **Fig. 3**
258 treated with eight different drugs, generating approximately 80 ToD profiles (**Fig. 4d,e** and
259 **Supplementary Fig. 4a,b**). Comparing examples from individual cell lines, namely HCC1937
260 and MCF10A, revealed that HCC1937 exhibited relatively conserved ToD profiles, whereas
261 the non-malignant cell line showed greater ToD variability for the different drugs (**Fig. 4d**).
262 Furthermore, ToD sensitivity profiles varied significantly from drug to drug (**Fig. 4e** and
263 **Supplementary Fig. 4b**), suggesting that ToD profiles may be highly dependent on the cancer
264 cell model and drug mechanism of action.
265 To assess varying time-of-day sensitivities across all tested cell line models and drugs, we
266 calculated the corresponding ToD_{MR} value for each drug-cell combination (**Fig. 4f**). Averaging
267 the ToD_{MR} values per drug and cell line revealed a gradual ranking of ToD variability for each
268 drug and cell model tested (**Fig. 4g**). Within the drug panel, the highest and lowest ToD
269 variability was observed for cisplatin and alisertib, respectively, with a ~2-fold difference in
270 the average ToD_{MR} value (**Fig. 4g,** *top panel*). Similarly, the ToD variability of the tested cell
271 lines varied by ~2-fold, with MCF10A showing the highest and HCC38 the lowest average
272 variability. Considering only cancer cell lines, SUM149PT ranked highest and showed a
273 similar degree of ToD sensitivity variability as the non-malignant cell line (**Fig. 4g**, *bottom*
274 *panel*).
275 Together, our findings reveal distinct ToD profiles across most tested drugs and models,
276 highlighting individualized ToD sensitivity within distinct drugs and cell models despite the
277 common TNBC categorization and shared drug-target pathways.
278

Determining treatment times for maximum drug effect

The critical factor in the design of future chronotherapeutic treatments may be not only be the sensitivity of cancer cells, but rather the differential time-of-day sensitivity between cancer and non-malignant tissues[26]. To illustrate this, we compared the ToD response profiles of TNBC cancer cell models with the profile of MCF10A, as shown for HCC1937 and alisertib in **Fig. 4h**. In this case, the cancer and non-malignant tissue models show an antiphasic ToD response profile, with an almost inverted profile. By calculating the greatest response differences between the two cell models, we determined the treatment times of maximum and minimum benefit (**Fig. 4h–j**). Analyzing the entire panel of tested drugs per cell line model and plotting polar density histograms of the times of maximum and minimum benefit, we found that highest overall benefit is achieved at 10–12 h and 18–20 h in the treatment of HCC1937, while earlier treatment times of the day yield minimum benefit. In contrast, SUM149PT and MDAMB231 show a single prominent time window throughout the day that provides maximum treatment benefit (**Fig. 4i**). In addition to cell model-to-model variability in the benefit times, we explored the drug-to-drug variability by calculating the polar density histogram for the individual drugs tested across all cell line models (**Fig. 4j**). 5-FU showed a clear preference for administration between 8 and 10 h, while torin2 and paclitaxel showed more variability in maximum and minimum benefit times, indicating different response relationships to the non-malignant tissue model across the cancer cell lines tested.

Finally, we quantified the extent of maximum and minimum treatment benefit by calculating the corresponding fold changes in ToD responses between the cancer and non-malignant tissue model (**Fig. 4k**). By averaging these fold changes across cell lines and drugs, we established a ranking referred to here as the "chronotherapeutic index". While the average ToD variability highlights the benefits of a single model (**Fig. 4g**), the chronotherapeutic index reveals distinctions between cancer and non-malignant models, thereby it is offering valuable insights into the potential advantages of adopting a chronotherapeutic-based schedule. It's worth noting that the rankings based solely on average ToD variability within a single model or drug didn't align completely with the ranking of the chronotherapeutic index. This emphasizes the importance of evaluating effects in relation to healthy tissues when considering chronotherapy applications (**Fig. 4g,k**).

To sum up, our findings emphasize distinct chronotherapeutic response dynamics in vitro between cancer and healthy tissue models, underscoring two key objectives of chronotherapy:

311 pinpointing optimal treatment times to maximize cancer toxicity while minimizing impacts on
312 healthy tissues.
313

314 The relationship between time-of-day profiles and clock, growth, and drug 315 sensitivity metrics

316 The time-of-day sensitivity in cancer models results from complex interactions involving the
317 circadian clock, cancer cell growth, and drug responses. However, the specific mechanisms
318 governing these interactions remain largely unknown. To address this, we employ statistical
319 tools, including linear regression, dominance analysis, and determinant ranking, to uncover the
320 key parameters influencing a key aspect of ToD sensitivity curves, namely the maximum range
321 in responses (ToD_{MR}) (**Fig. 5a**). To explore how individual metrics relate to ToD_{MR} values, we
322 first performed pairwise linear regression analysis (**Fig. 5b–f**). We considered each circadian
323 channel individually or combined and found the strongest and most significant correlations for
324 clock metrics from the *Bmal1* channel (**Fig. 5d** and **Supplementary Fig. 5a**). ToD_{MR} values of
325 5-FU were significantly correlated with amplitudes (r=0.8, R^2=0.6) and the prominence of
326 circadian component (circadianicity) of the *Bmal1* signal (r=0.7, R^2=0.43), whereas other
327 circadian clock metrics were poorly associated (**Fig. 5b**,**d**). On the other hand, we observed no
328 significant and rather low associations for ToD_{MR} values and growth metrics as well as for
329 ToD_{MR} values and drug sensitivity metrics (**Fig. 5c,e,f**). To identify the best associated
330 individual metric and drug, we integrated all correlations and generated a ranking as shown in
331 **Fig. 5g**. For the different metrics, we observed the highest correlation for the amplitude
332 (r=0.43±0.02, mean ± s.e.m.). Among the individual drugs, adavosertib ranked highest in
333 overall correlation (r=0.39±0.03, mean ± s.e.m.) between ToD_{MR} values and the different
334 metrics. Relative average associations between all metrics and ToD_{MR} values were
335 predominantly positive, with only five metrics demonstrating inverse relationships
336 (**Supplementary Fig. 5b**). Notably, only one drug, paclitaxel, displayed average negative
337 associations across all metrics.
338 While linear regression approaches are robust for examining individual metrics, they do not
339 provide relative information about which metrics have the most significant impact on ToD_{MR}
340 values. To address this, we used dominance analysis and systematically tested all possible
341 combinations of metrics. By measuring how much each metric improved the accuracy of the

342 model when added or removed, we identified the most important predictors of ToD_{MR} values
343 to the different drugs. For alpelisib our analysis identified high predictive power for the
344 amplitude of *Bmal1* signals, contributing 42% of the observed ToD sensitivity variability (**Fig.**
345 **5h**). In contrast, paclitaxel and adavosertib showed the most homogeneous distribution of
346 individual contributions, with no metric appearing to have a dominant predictive power.
347 Considering the shares of each determinant combined for all drugs led to a ranking of
348 determinants as shown in **Fig. 5i**. Here, we observed the largest contributions for the *Bmal1*
349 amplitude (mean = 21.9%) and smallest for the Hill coefficient of drug response curves (mean
350 = 9.9%).
351 In summary, we were able to identify systematic dependencies of the maximal time-of-day
352 drug sensitivities and different circadian clock, growth and drug sensitivity parameters. We
353 have further shown that the predictive power of the different determinants varies substantially
354 depending on the specific drug, highlighting the importance of considering multiple factors in
355 understanding the time-of-day dependent variability of drug response in a cell model.
356

357 Differential impact of core clock genes in shaping time-of-day sensitivity of 358 cancer models

359 Beyond a cancer model's circadian clock, growth, and drug features, the expression levels of
360 core circadian clock genes are likely to contribute the time-of-day sensitivity profiles. Thus,
361 we explored the connection between the expression patterns of 16 essential clock genes and
362 the maximum range of ToD sensitivity profiles (ToD_{MR}). We defined core clock genes as those
363 that directly control the transcriptional-translational feedback loops of the molecular clock
364 network and whose dysregulation or mutations result in disrupted circadian rhythms[31,32]. The
365 selected gene panel displayed distinct expression patterns across the TNBC cell lines tested
366 (**Supplementary Fig. 6a**). To examine potential relationships between core clock genes and
367 ToD_{MR} values, we used three different methods, namely linear correlation analysis,
368 dimensionality reduction by linear discriminant analysis (LDA) and principal component
369 analysis (PCA) (**Fig. 6a**).
370 Linear correlation analysis revealed significant correlations between the ToD_{MR} values from
371 our panel of tested drugs and several of the core clock genes, suggesting potential links between
372 the circadian clock machinery and drug sensitivity (**Fig. 6b**). Focusing on the mitosis inhibitor

373 paclitaxel, we identified particularly strong anticorrelations with the expression levels of *Per3*
374 (r=-0.88, R^2=0.78) and *Dbp* (r=-0.72, R^2=0.51) (**Fig. 6b,c**). Accumulating absolute
375 correlations of each drug for all circadian clock genes revealed highest overall correlation of
376 ToD_{MR} values for cisplatin (r=0.40±0.21, mean ± s.d.), while *Per2* was most associated with
377 ToD_{MR} values among the circadian clock gene panel (r=0.48±0.20, mean ± s.d.) (**Fig. 6d**).
378 To test if our gene set could broadly categorize the strength of time-of-day effects as indicated
379 by the ToD_{MR} values, we next turned to LDA analysis in a drug-by-drug basis. To do so, we
380 first categorized cell models into two groups based on the median ToD_{MR} value for each drug.
381 **Fig. 6e** provides an example using paclitaxel, effectively separating the data into groups with
382 high and low ToD_{MR} values. Implementing LDA to examine the individual linear discriminant
383 components of each circadian clock gene revealed a clear ranking of genes in terms of their
384 importance in discriminating the cell lines into the two ToD_{MR} groups. For paclitaxel, the core
385 clock genes *Cry2*, *Dbp*, and *Per3* were the most important contributors to the specific
386 discrimination, collectively accounting for approximately 46% of the discriminative
387 information (**Fig. 6e**, *right panel*). Importantly, the contribution of each gene in discriminating
388 between ToD_{MR} responses varied for the different drugs, suggesting that each drug interacts
389 differently with the molecular components of the circadian clock (**Supplementary Fig. 6b–h**).
390 To explore the circadian clock's impact on ToD sensitivity across various drug treatments, we
391 assessed the overall contribution of each gene by cumulating their effects across all drugs.
392 Here, *Rorβ* exhibited the overall highest contribution, accounting for 10.5% ± 9.6% (mean ±
393 s.d.) of the discriminative information (**Fig. 6f**).
394 While LDA is a powerful method to determine the discriminatory contribution of the individual
395 core clock genes, PCA allows for identifying underlying patterns and relationships among the
396 different genes. For paclitaxel, PCA distributed the cell models well along the first two
397 principal components which combined explained 73.7% of the variability among the different
398 ToD sensitivity profiles (**Supplementary Fig. 6i**, *left panel*). Ranking of the PC loadings
399 showed that the degree of contribution of each circadian clock gene in shaping the PCA
400 outcome was highly individual. For paclitaxel, *Csnk1d* was the major contributor to the ToD
401 sensitivity variability within the first principal component, while along the second principal
402 component, *Clock* ranked as main contributor (**Supplementary Fig. 6i**, *right panels*).
403 Collectively, our findings suggest associations between the expression levels of core clock
404 genes and the observed ToD maximum ranges within the examined cell lines. These results

underscore potential connections between the molecular circadian clock and time-of-day drug responses.

Discussion

While the fundamental role of the circadian clock in influencing disease progression and treatment response is widely recognized[22,33,34], our understanding of the underlying biological mechanisms remains fragmented. Approaches that enable the precise study of drug-perturbations and treatment responses within controlled circadian-timed environments play a pivotal role in advancing our understanding of the effects regulated by the circadian clock. To date, there has been a notable absence of standardized methodologies for the comprehensive exploration of the chronotherapeutic potential of drugs and cancer models. In this work we present an integrative approach for the high-throughput quantification of time-of-day response profiles and the elucidation of circadian, growth and drug sensitivity factors that shape these profiles (**Fig. 1**). This innovative method holds significant promise for advancing biological discovery, offering a robust platform to explore the intricate interplay between circadian rhythms, cellular growth, and drug timing efficacy.

Despite the general expectation that the circadian clock is likely dysregulated in highly transformed cancers[19,33], our approach reveals robust rhythms in numerous cancer cell models, whose circadian properties were previously unknown (**Fig. 2**). Furthermore, our assessment of circadian rhythms in non-malignant epithelial cells, luminal breast cancer cells, and osteosarcoma cells aligns with prior research[28,35-37], underscoring the versatility of our approach in elucidating circadian clock properties across various cancer and tissue types.

Among these, we focused on triple-negative breast cancer, a highly aggressive and heterogeneous subtype, representing about 15% of diagnosed breast tumors. Current therapies are ineffective, with cytotoxic chemotherapy still being an integral part of treatment despite limited efficacy and severe side effects[38]. Our investigation into the growth dynamics and drug responses of multiple TNBC cell models has generated a diverse array of metrics. Notably, in agreement with recent studies[39], our results indicate that the sensitivity metrics exhibit milder correlations, challenging the conventional binary classification of sensitive versus resistant models and suggesting that drug sensitivity rankings are rather metric-specific and drug-dependent (**Fig. 3**).

436 By implementing our screening approach for the profiling of drug sensitivities across different
437 times of the day, we generated approximately 80 distinct time-of-day profiles, unveiling a wide
438 range of sensitivity variations across drugs and cell line models (**Fig. 4** and **Supplementary**
439 **Fig. 4**). We then ranked models by their time-of-day sensitivity and observed up to 30%
440 response differences throughout the day for the top scoring models. We further detected
441 substantial variation in time-of-day sensitivity among the panel of drugs tested, revealing
442 previously unknown time-of-day dependent drug effects. Consistent with previous findings,
443 we show time-of-day dependent variability in responses to the DNA synthesis inhibitors 5-FU
444 and doxorubicin as well as to the DNA intercalator cisplatin[22]. Furthermore, we have
445 introduced a novel chronotherapeutic index, which gauges the relative advantages of adopting
446 a circadian-based drug schedule. Various non-malignant tissue models may be employed for
447 calculating this index, tailored to the particular disease model under investigation. For example,
448 fibroblast models, whose strong circadian rhythms have been described in several works[40-42],
449 are expected to show unique relationships with cancer models in terms of sensitivity patterns
450 at different times of the day.
451 Delving into the intricate molecular mechanisms that potentially govern time-of-day
452 sensitivity, our novel method has unraveled key relationships between circadian clock
453 dynamics, growth patterns, and drug sensitivities, all of which significantly impact time-of-day
454 drug responses. It is noteworthy that the specific contribution of these parameters varies
455 depending on the particular drug under consideration, underscoring the multifactorial nature of
456 time-of-day dependent variability in drug reactions (**Fig. 5**). Furthermore, our exploration has
457 shed light on the involvement of core circadian clock genes in this context, hinting at potential
458 connections between the molecular circadian clock network and ToD drug sensitivity (**Fig. 6**).
459 While our findings are primarily based on in vitro models and are not directly applicable for
460 treatment recommendations, our framework can be directly applied to model organisms of
461 higher complexity, such as 3D patient-derived organoids and animal models where the
462 circadian clock can be tracked. Furthermore, additional research is needed to discern the
463 relative contributions of the cell cycle and circadian clock to the observed ToD sensitivity[40,43-
464 45].
465 Altogether, we provide a comprehensive method to determine optimal drug treatment times of
466 complex diseases and to identify the cell subtypes that will most benefit from a time-of-day
467 based treatment. Leveraging innovative experimental and computational techniques our

approach further elucidates the specific biological features that shape time-of-day response profiles, thereby advancing our understanding of the cellular mechanisms that drive time-of-day sensitivity. As a result, our method provides tools to uncover the cellular mechanisms that govern time-of-day sensitivity, paving the way for new biological discoveries.

Acknowledgements

We would like to thank Malthe Skytte Nordentoft Nielsen as well as the laboratories of Michela Di Virgilio and Ingeborg Tinhofer-Keilholz for their valuable feedback to our project. We would also like to thank Annika Winkler for her assistance with sample preparation. The results are part of a project funded by the German Federal Ministry of Education and Research (BMBF) through the e:Med Juniorverbund DeepLTNBC TP3-01ZX1917C. C.E. was partially supported by the Deutsche Forschungsgemeinschaft (DFG, German Research Foundation)–RTG2424/CompCancer – project number: 377984878 and is enrolled in the doctoral program of the Berlin School of Integrative Oncology (BSIO). C.S. acknowledges support from the DFG–SCHM 3362/4–1 project number: 511886499.

Materials and Methods

Experimental methods

Cell culture

HCC1143, HCC1806, HCC1937, HCC38, and MDAMB468 cells were obtained from the American Type Culture Collection. CAL51, MDAMB231, MDAMB436 and SUM149PT cells were kindly provided by the Sorger lab (Harvard Medical School, Ludwig Cancer Center, Boston, USA). MCF10A and MCF7 cells were kindly gifted by the Brugge lab (Harvard Medical School, Ludwig Cancer Center, Boston, USA). GIMEN and SH-SY5Y cells were provided by the Schulte lab (Universitätsklinikum Tübingen, Clinic for Pediatrics and Adolescent Medicine, Thübingen, Germany) and the U-2 OS reporter cell lines by the Kramer lab (Charité, Institute for Medical Immunology, Berlin, Germany). MCF10A cells were maintained according to the Brugge lab's media recipe based on DMEM/F12 media (Gibco)

496 supplemented with 5% horse serum (Gibco), 20 ng/ml EGF (Peprotech), 0.5 mg/ml
497 Hydrocortisone (Sigma), 100 ng/ml Cholera Toxin (Sigma), 10 µg/ml Insulin (Sigma) and 1%
498 penicillin-streptomycin (Pen-Strep, Gibco). All other cell lines were maintained in RPMI 1640
499 (Gibco) supplemented with 10% fetal bovine serum (FBS) (Gibco) and 1% Pen-Strep. For
500 bioluminescence recordings and long-term imaging, cells were cultured in FluoroBrite DMEM
501 medium (Gibco) supplemented with 10% FBS, 300 mg L-Glutamine (Gibco) and 1% Pen-
502 Strep. Cells were kept at 37 °C in a humidified 5% CO_2 environment and regularly tested for
503 mycoplasma.

504 Generation of reporter cell lines

505 To produce lentivirus carrying constitutive red-fluorescent nuclear reporters, HEK293T cells
506 at 80% confluence were transfected with a mix of 1.8 µg gag/pol packaging plasmid (Addgene
507 #14887), 0.7 µg pRev packaging plasmid (Addgene #12253), 0.3 µg VSV-G envelope plasmid
508 (Addgene #14888) and 3.2 µg of a plasmid with a EF1α-mKate2-NLS sequence. Lentivirus
509 expressing either *Bmal1*- or *Per2*-promoter driven luciferase reporter was produced by
510 transfecting HEK293T cells with 6 µg psPAX2 (Addgene #12260), 3.6 µg pMD2G (Addgene
511 #12259) and 8.4 µg lentiviral expression plasmid (pAB-mBmal1:Luc-Puro or plenti6-
512 mPer2:Luc-Blast, respectively). Transfections were conducted using Lipofectamine 3000
513 (Invitrogen) according to the manufacturer's instructions and media was replaced by RMPI
514 1640 medium supplemented with 10 mM HEPES before adding the transfection mixture.
515 Lentiviral supernatant was collected after 48 h and 72 h and passed through a 0.45 µm filter
516 (Millipore). For lentiviral transduction, receiver cells at 70% confluence were incubated with
517 a mix of 1 ml lentivirus-containing supernatant, 8 µg/ml protamine sulfate (Sigma) and 10 µM
518 HEPES (Gibco) for 6 h. Ensuing, cells were washed with PBS (Gibco) and cultured in their
519 regular culture medium for 2 days before starting antibiotic selection of transduced cells. To
520 select for transduced cells, cells were grown in medium containing 5 µg/ml blasticidin (Adooq)
521 or 2 µg/ml puromycin (Gibco) according to the resistance cassette on the lentiviral expression
522 plasmid until non-transduced control cells died. Details about the generation of the U-2 OS-
523 *Cry1*-sKO and U-2 OS-*Cry1*/*Cry2*-dKO cell lines can be found in the original publication by
524 Börding *et al.*[28].

525 ## Bioluminescence recordings

526 Cells expressing *Bmal1*- or *Per2*-promoter driven luciferase reporters were seeded in 35-mm
527 dishes (Nunc) to reach approximate confluence on the following day. To account for potentially
528 different phases of single-cell circadian clocks in cell populations, we collectively reset the
529 circadian clocks by administering a standard dose of 1 µM dexamethasone[46,47] (Sigma,
530 dissolved in EtOH). After 30 min incubation cells were washed once with PBS and imaging
531 medium supplemented with 250 µM D-Luciferin (Abmole) was added. To avoid evaporation
532 of the media throughout the bioluminescence recordings, the dishes were sealed with parafilm
533 as described in Finger *et al.*[46]. Luminescence intensity was monitored at 10-min intervals for 5
534 days in an incubator-embedded luminometer (LumiCycle, Actimetrics).

535 ## Long-term live-cell imaging

536 All live-cell imaging experiments were performed with cells expressing the fluorescent
537 mKate2-NLS nuclear reporter, seeded in 48-well plates (Falcon) at a density that saturates at
538 unperturbed growth conditions towards the end of each experiment. Long-term live-cell
539 imaging was conducted using an incubator-embedded Incucyte live-cell widefield microscope
540 (Essen BioScience). Cells were imaged in the brightfield and for nuclei segmentation and cell
541 counting in the red channel (excitation: 567–607 nm, emission: 622–704 nm). Images were
542 analyzed by frame-by-frame nuclei counting with the in-built Incucyte software and results
543 were further processed in MATLAB. For experiments that involved drug treatments, cells were
544 seeded 1 day before starting the live recordings and images were taken using a 4x magnification
545 lens in 2 fields-of-views per well every 1–2 h for a total duration of 4–6 days. Two independent
546 plates per condition were assayed. For drug response experiments with cisplatin a single plate
547 per condition was assayed, imaged in 9 fields-of-views using a 10x magnification lens. For
548 experiments capturing unperturbed growth dynamics, 300–1000 cells, corresponding to ~10%
549 confluency, were seeded 2 days before starting the live recordings. Using a 10x magnification
550 lens, 9 images per well were acquired in 1–2 h intervals for a total duration of 4 days.

551 ## Dose-response curves

552 Drug stock solutions (100–10 mM) were prepared in DMSO and preserved at -20°C. Cisplatin
553 (Sigma) stock solution of 3.33 mM was prepared in 0.9% NaCl and stored at room temperature.

554 For dose-response assays, a serial 5–6 point log4 dilution of each drug was freshly prepared in
555 its solvent prior to treatment. Following concentration ranges were tested: 100–0.1 µM for 5-
556 fluorouracil (5-FU, Sigma), alpelisib (Biozol) and olaparib (Adooq); 10–0.01 µM for torin2
557 (Sigma) and alisertib (Hölzel); 10–0.04 µM for adavosertib (Biocat); 1–0.004 µM for
558 doxorubicin (Hölzel); and 0.4–0.0004 µM for paclitaxel (Hölzel). Cisplatin was tested in a
559 serial 10-point log2 dilution with doses ranging from 70–0.14 µM. Compounds were added to
560 the cells one day after cell seeding in a drug-media mixture of 9% of total well-volume.
561 Solvent-only treated control cells were assayed along the treated conditions. Each tested
562 condition contained equal amounts of the solvent. Cell growth was monitored by live-cell
563 imaging for at least 4 days as described above.

564 Time-of-day treatments

565 Cells were seeded and allowed to attach overnight. The next day, live recordings commenced
566 as described earlier. We performed independent resetting steps every 4 h over an 8-h period,
567 creating distinct cell populations at 0, 4, or 8 h of circadian time. Subsequently, we
568 administered the same drug concentration, which corresponded to the estimated half-maximal
569 effective concentration, at either 32 or 48 h after the initial resetting step. This allowed us to
570 simultaneously test six different circadian stages (0, 4, 8, 16, 20, and 24 h). Drug concentrations
571 were determined separately for each cell line and drug combination. For cisplatin, the
572 treatments we performed slightly different, using 4 independent resetting steps every 3 hours
573 over a 9-h period followed by drug treatments 32 or 48 h post initial resetting. In all cases, cell
574 growth was continuously monitored through long-term live-cell imaging for a total of 6 days.

575 Computational methods

576 Time-series analysis of circadian signals

577 **Detrending.** Raw time-series data were detrended by applying a sinc filter with a 48-h cut-off
578 period using the open-source software package pyBOAT[27] (v0.9.1) within the Anaconda
579 Navigator (v1.10.0).
580 **Amplitude envelope and normalization**. Continuous amplitude envelope calculation was
581 obtained using continuous wavelet transform implemented in pyBOAT with a time window of

582 48 hours. The amplitude normalization was done by taking the inverse of the envelope of the
583 detrended signal as describe in Mönke G, *et al.* [27] .
584 **Autocorrelation analysis.** Periodicity data was assessed by calculating its autocorrelation and
585 abcissa at the second peak using the 'autocorr' and 'findpeaks' MATLAB functions[48] from the
586 detrended time-series.
587 **Continuous wavelet transform.** The main oscillatory component, known as the ridge
588 component, was obtained using a wavelet-based spectral analysis from amplitude-normalized
589 and detrended signals. For the ridge detection we used both an adaptable-threshold and a fixed-
590 threshold. The adaptable-threshold was based on each signal's half-maximal spectral power
591 and was implemented for the "ridge length" metric shown in Fig. 2. The instantaneous phase
592 difference between the *Bmal1* and *Per2* signals was calculated using the MATLAB 'atan2'
593 function (Supplementary Fig. 1a) and for the polar histogram representation, we deployed the
594 'polarhistogram' function from MATLAB (Supplementary Fig. 1b). For the analysis of
595 determinants for time-of-day sensitivity shown in Fig. 5, the metrics of the main oscillatory
596 component were derived using a fixed-ridge threshold of 40. This ridge threshold value was
597 chosen as it offered a well-balanced threshold suitable for comparing signals of varying
598 strengths.
599 **Multiresolution analysis.** Detrended time-series data were decomposed into a set of different
600 wavelet details D_j representing distinct disjoint frequency bands and a final smooth using a
601 discrete wavelet transform based multiresolution analysis[49]. The algorithm has been
602 implemented using the 'PyWavelets' python package[50], with a *db20* wavelet of the Daubechies
603 wavelet family as previously described in Myung, Schmal and Hong *et al.*[51]. Since each
604 wavelet detail D_j represents a period range between $2^j\Delta t$ and $2^{j+1}\Delta t$ (for j=1, 2, 3, …) we down-
605 sampled the time series from a Δt=10 min to a Δt=30 min sampling frequency to obtain a
606 circadian period band between 16–32 h for further analysis. Since the MRA decomposes the
607 variance of the detrended signal with respect to the different disjoint period bands it can be
608 used to determine the rhythmicity of the signal in the circadian period range[52].
609 **Global circadian strength.** To calculate the global circadian strength (*GCS*) of a cell line
610 model *i*, the autocorrelation peak value (peak), the wavelet-based continuous ridge length
611 (ridge) and the discrete circadianicity component (circadianicity) were normalized to the
612 respective maximum (max) value measured among all tested cell line models and averaged
613 according to the following equation:

614 $$GCS_i = \text{mean}\left(\frac{\text{peak}_i}{\text{peak}_{\text{max}}}, \frac{\text{ridge}_i}{\text{ridge}_{\text{max}}}, \frac{\text{circadianicity}_i}{\text{circadianicity}_{\text{max}}}\right)$$

615 **Statistical analysis.** Linear regression model fitting of *Bmal1* and *Per2* circadianicity
616 components obtained by MRA was done with the 'fitlm' MATLAB function. Significant
617 differences in circadian parameters between knockout and wild-type U-2 OS cells were
618 calculated with a two-sample *t*-test using the 'ttest2' MATLAB function.

619 Multi-parametric analysis of growth dynamics

620 Growth data obtained from long-term live-cell imaging was smoothed using a robust local
621 regression approach of weighted linear least squares and a 2nd degree polynomial model
622 ('rloess' MATLAB function). Doubling times of smoothed cell numbers or confluency were
623 calculated according to the following equation:

624 $$\text{Doubling time}(t) = t * \frac{\log(2)}{\log(y_0/y_t)}$$

625 where t refers to the time of assessment, in our case 96 h, and y_0 refers to the cell number at
626 timepoint 0. To calculate the exponential growth rate k per unit of time t, we normalized cell
627 numbers to the initial timepoint 0 (y_0) and fitted an exponential function to the growth curves:

628 $$\text{Growth}(t) = y_0 * e^{(k*t)}$$

629 Exponential function fitting was done with the MATLAB 'fit' function[48]. Linear regression
630 model fitting to different combinations of growth parameters was done with the 'fitlm'
631 MATLAB function.

632 Estimation of drug sensitivity parameters

633 Drug response data obtained from long-term live-cell imaging was smoothed using a robust
634 local regression approach of weighted linear least squares and a 2nd degree polynomial model
635 ('rloess' MATLAB function). Following the method established by Hafner *et al.*[30], we
636 computed the growth rate inhibition (*GR*) at time *t* and for each dose *c* as follows:

637 $$GR(c,t) = 2^{k(c,t)/k(0)} - 1$$

638 where $k(c,t)$ is the growth rate under drug treatment and $k(0)$ is the growth rate of untreated
639 cells. Drug response parameters were retrieved by fitting the dose-dependent *GR* values to a
640 sigmoid curve using the following equation:

641 $$GR(c) = GR_{\text{inf}} + \frac{1 - GR_{\text{inf}}}{1 + (c/GEC_{50})^{h_{\text{GR}}}}$$

642 where the fitted parameters are as described in Hafner *et al.*[30]. Standard EC_{50} values were
643 calculated by fitting final nucleus counts, normalized to the respective count of the control, to
644 the following sigmoidal function:

645 $$f(c) = E_{\text{min}} + \frac{1 - E_{\text{min}}}{1 + (c/EC_{50})^{h}}$$

646 where E_{min} corresponds to the minimum response, restricted to values between 0 and 1, and h
647 is the hill slope of the response curve, constrained to 0.5–10. Sigmoidal function fitting steps
648 were done with the MATLAB functions 'fit' (*GR* metrics) or 'lsqnonlin' (EC_{50} value)[48].
649 Hierarchical clustering analysis was implemented with the MATLAB 'clustergram' function
650 using an euclidian distance and average linkage method[48]. To account for the different tested
651 dose ranges across drugs for clustering, GEC_{50} values were normalized to the dose at GR_{inf}.
652 Pearson's linear correlation coefficients across drug sensitivity metrics were computed using
653 the MATLAB 'corr' function. For the comparison of cellular growth dynamics to drug doses
654 evoking the maximum tested effect, we chose growth curves corresponding to the doses closest
655 to the determined GR_{inf} values.

656 Time-of-day sensitivity evaluation

657 Drug response data of time-of-day treatment experiments was smoothed using a moving
658 average ('smoothdata' MATLAB function). Final nucleus counts were normalized to the
659 nucleus count at the respective time of treatment. Time-of-day response curves were generated
660 from the relative final nucleus counts of each treatment timepoint to the final nucleus count at
661 timepoint 0 and interpolated using the 'smoothingspline' function in MATLAB. The
662 smoothing parameter was set to 0.7. The maximum range across smoothed time-of-day
663 responses (ToD_{MR}) was calculated by subtraction of the minimum from the maximum relative
664 response. To assess whether the smoothing of response data introduces artifacts into ToD_{MR}

665 estimates, we performed linear regression analysis between ToD_{MR} values from raw and spline
666 smoothed data using the 'fitlm' MATLAB function and confirmed a high positive correlation
667 (**Supplementary Fig. 7**). ToD_{MR} values were clustered as described for the drug sensitivity
668 parameters, with missing data points substituted by values from the closest relevant column,
669 adhering to the 'nearest-neighbor' principle. Polar histograms of the treatment times with
670 maximum and minimum benefit were generated using the 'polarhistogram' MATLAB function
671 with 'probability' normalization to depict each bar's height as the fraction of observations
672 within its bin relative to the total observations.

673 Correlation and shapley value regression analysis

674 Linear regressions of cell-intrinsic features and drug-dependent ToD sensitivity have been
675 obtained using the 'stats' and 'optimize' modules of the 'SciPy' and the 'uncertainties' package
676 of the Python programming language. The relative importance of the different predictors in a
677 multiple linear regression model are obtained by Shapley value regression via the Python
678 'dominance-analysis' package.

679 Circadian clock gene expression analysis

680 Gene expression data of circadian clock genes were obtained from the Cancer Cell Line
681 Encyclopedia Dependency Map (CCLE DepMap, https://sites.broadinstitute.org/ccle/datasets,
682 Q4 of 2022)[53]. Circadian clock genes of the individual breast cancer cell lines were clustered
683 using the 'clustermap' plotting function of 'seaborn' with the euclidian distance metric and
684 complete linkage method. Spearman rank correlation coefficients of circadian clock genes and
685 drug-specific ToD sensitivity values were computed using the spearman rank correlation
686 algorithm of the 'SciPy stats' python language module and hierarchically clustered with the
687 correlation distance metric and single linkage method. Regression plots were obtained using
688 the 'jointplot' plotting function from 'seaborn', showing drug-specific correlation between the
689 ToD sensitivities and gene expression of each cell line, including their distribution, squared
690 spearman rank correlation coefficient, *p*-value, and a confidence interval of 95%.

691 ## Supervised and unsupervised dimensionality reduction

692 Supervised dimensionality reduction by linear discriminant analysis was performed with the
693 'LinearDiscriminantAnalysis' function of the 'sklearn discriminant_analysis' python language
694 module. The default parameters were retained, using the exact full singular value
695 decomposition solver and 1 component. Median-based binarization of the drug-dependent ToD
696 sensitivity values were used as target and the resulting linear discriminant vector was plotted
697 using random y-axis units to avoid overlapping of the data points. The contribution to the
698 obtained discriminative information is shown in percentage for each of the circadian clock
699 genes. Unsupervised dimensionality reduction by principal component analysis (PCA) was
700 performed with the 'PCA' function of the 'sklearn decomposition' python language module
701 using the exact full singular value decomposition solver and number of components equivalent
702 to the sample size of the corresponding drug. Further analysis of the most informative PCA
703 components was done by drawing the biplots of the first two principal components and showing
704 the loadings of each circadian clock gene for both components.
705

706 ## Data availability

707 The experimental time series data and data tables for all results of this study are available upon
708 request.
709

710 ## Code availability

711 Code used for the data analysis in this work is available upon request.
712

713 ## Competing interests

714 The authors declare no competing interests.
715

716 **References**

717 1 Chaix, A., Zarrinpar, A. & Panda, S. The circadian coordination of cell biology. *J Cell Biol*
718 **215**, 15-25, doi:10.1083/jcb.201603076 (2016).

719 2 Zhang, R., Lahens, N. F., Ballance, H. I., Hughes, M. E. & Hogenesch, J. B. A circadian gene
720 expression atlas in mammals: implications for biology and medicine. *Proc Natl Acad Sci U S*
721 *A* **111**, 16219-16224, doi:10.1073/pnas.1408886111 (2014).

722 3 Mure, L. S. *et al.* Diurnal transcriptome atlas of a primate across major neural and peripheral
723 tissues. *Science* **359**, doi:10.1126/science.aao0318 (2018).

724 4 Saini, C. *et al.* A functional circadian clock is required for proper insulin secretion by human
725 pancreatic islet cells. *Diabetes, Obesity and Metabolism* **18**, 355-365,
726 doi:https://doi.org/10.1111/dom.12616 (2016).

727 5 Neufeld-Cohen, A. *et al.* Circadian control of oscillations in mitochondrial rate-limiting
728 enzymes and nutrient utilization by PERIOD proteins. *Proc Natl Acad Sci U S A* **113**, E1673-
729 1682, doi:10.1073/pnas.1519650113 (2016).

730 6 Chakrabarti, S. & Michor, F. Circadian clock effects on cellular proliferation: Insights from
731 theory and experiments. *Current Opinion in Cell Biology* **67**, 17-26,
732 doi:https://doi.org/10.1016/j.ceb.2020.07.003 (2020).

733 7 Scheiermann, C., Kunisaki, Y. & Frenette, P. S. Circadian control of the immune system.
734 *Nature Reviews Immunology* **13**, 190-198, doi:10.1038/nri3386 (2013).

735 8 Sancar, A. *et al.* Circadian clock control of the cellular response to DNA damage. *FEBS Lett*
736 **584**, 2618-2625, doi:10.1016/j.febslet.2010.03.017 (2010).

737 9 Schernhammer, E. S. *et al.* Rotating night shifts and risk of breast cancer in women participating
738 in the nurses' health study. *J Natl Cancer Inst* **93**, 1563-1568, doi:10.1093/jnci/93.20.1563
739 (2001).

740 10 Puram, Rishi V. *et al.* Core Circadian Clock Genes Regulate Leukemia Stem Cells in AML.
741 *Cell* **165**, 303-316, doi:10.1016/j.cell.2016.03.015 (2016).

742 11 Papagiannakopoulos, T. *et al.* Circadian Rhythm Disruption Promotes Lung Tumorigenesis.
743 *Cell Metab* **24**, 324-331, doi:10.1016/j.cmet.2016.07.001 (2016).

744 12 Chun, S. K. *et al.* Disruption of the circadian clock drives Apc loss of heterozygosity to
745 accelerate colorectal cancer. *Science Advances* **8**, eabo2389, doi:doi:10.1126/sciadv.abo2389
746 (2022).

747 13 Diamantopoulou, Z. *et al.* The metastatic spread of breast cancer accelerates during sleep.
748 *Nature* **607**, 156-162, doi:10.1038/s41586-022-04875-y (2022).

14 Wang, J. *et al.* Circadian protein BMAL1 promotes breast cancer cell invasion and metastasis by up-regulating matrix metalloproteinase9 expression. *Cancer Cell International* **19**, 182, doi:10.1186/s12935-019-0902-2 (2019).

15 Lee, Y. *et al.* G1/S cell cycle regulators mediate effects of circadian dysregulation on tumor growth and provide targets for timed anticancer treatment. *PLOS Biology* **17**, e3000228, doi:10.1371/journal.pbio.3000228 (2019).

16 Chen, W.-D. *et al.* The circadian rhythm controls telomeres and telomerase activity. *Biochemical and Biophysical Research Communications* **451**, 408-414, doi:https://doi.org/10.1016/j.bbrc.2014.07.138 (2014).

17 Rida, P., Syed, M. I. & Aneja, R. Time will tell: Circadian clock dysregulation in triple negative breast cancer. *Front Biosci (Schol Ed)* **11**, 178-192 (2019).

18 Innominato, P. F. *et al.* Prediction of overall survival through circadian rest-activity monitoring during chemotherapy for metastatic colorectal cancer. *International Journal of Cancer* **131**, 2684-2692, doi:https://doi.org/10.1002/ijc.27574 (2012).

19 Ye, Y. *et al.* The Genomic Landscape and Pharmacogenomic Interactions of Clock Genes in Cancer Chronotherapy. *Cell Systems* **6**, 314-328.e312, doi:https://doi.org/10.1016/j.cels.2018.01.013 (2018).

20 Lee, Y. *et al.* Time-of-day specificity of anticancer drugs may be mediated by circadian regulation of the cell cycle. *Science Advances* **7**, eabd2645, doi:10.1126/sciadv.abd2645 (2021).

21 Dallmann, R., Brown, S. A. & Gachon, F. Chronopharmacology: New Insights and Therapeutic Implications. *Annual Review of Pharmacology and Toxicology* **54**, 339-361, doi:10.1146/annurev-pharmtox-011613-135923 (2014).

22 Lévi, F., Okyar, A., Dulong, S., Innominato, P. F. & Clairambault, J. Circadian Timing in Cancer Treatments. *Annual Review of Pharmacology and Toxicology* **50**, 377-421, doi:10.1146/annurev.pharmtox.48.113006.094626 (2010).

23 Wood, P. A., Du-Quiton, J., You, S. & Hrushesky, W. J. M. Circadian clock coordinates cancer cell cycle progression, thymidylate synthase, and 5-fluorouracil therapeutic index. *Molecular Cancer Therapeutics* **5**, 2023-2033, doi:10.1158/1535-7163.Mct-06-0177 (2006).

24 Damato, A. R. *et al.* A randomized feasibility study evaluating temozolomide circadian medicine in patients with glioma. *Neuro-Oncology Practice* **9**, 193-200, doi:10.1093/nop/npac003 (2022).

25 Ruben, M. D., Smith, D. F., FitzGerald, G. A. & Hogenesch, J. B. Dosing time matters. *Science* **365**, 547-549, doi:doi:10.1126/science.aax7621 (2019).

26 Kramer, A. *et al.* Foundations of circadian medicine. *PLOS Biology* **20**, e3001567, doi:10.1371/journal.pbio.3001567 (2022).

785 27 Mönke, G., Sorgenfrei, F. A., Schmal, C. & Granada, A. E. Optimal time frequency analysis
786 for biological data - pyBOAT. *bioRxiv*, 2020.2004.2029.067744,
787 doi:10.1101/2020.04.29.067744 (2020).

788 28 Börding, T., Abdo, A. N., Maier, B., Gabriel, C. & Kramer, A. Generation of Human CRY1
789 and CRY2 Knockout Cells Using Duplex CRISPR/Cas9 Technology. *Front Physiol* **10**, 577,
790 doi:10.3389/fphys.2019.00577 (2019).

791 29 Leise, T. L. Analysis of Nonstationary Time Series for Biological Rhythms Research. *J Biol*
792 *Rhythms* **32**, 187-194, doi:10.1177/0748730417709105 (2017).

793 30 Hafner, M., Niepel, M., Chung, M. & Sorger, P. K. Growth rate inhibition metrics correct for
794 confounders in measuring sensitivity to cancer drugs. *Nature Methods* **13**, 521-527,
795 doi:10.1038/nmeth.3853 (2016).

796 31 Ko, C. H. & Takahashi, J. S. Molecular components of the mammalian circadian clock. *Hum*
797 *Mol Genet* **15 Spec No 2**, R271-277, doi:10.1093/hmg/ddl207 (2006).

798 32 Takahashi, J. S. Transcriptional architecture of the mammalian circadian clock. *Nature Reviews*
799 *Genetics* **18**, 164-179, doi:10.1038/nrg.2016.150 (2017).

800 33 Mormont, M.-C. & Levi, F. Cancer chronotherapy: Principles, applications, and perspectives.
801 *Cancer* **97**, 155-169, doi:https://doi.org/10.1002/cncr.11040 (2003).

802 34 Sulli, G., Lam, M. T. Y. & Panda, S. Interplay between Circadian Clock and Cancer: New
803 Frontiers for Cancer Treatment. *Trends in Cancer* **5**, 475-494,
804 doi:https://doi.org/10.1016/j.trecan.2019.07.002 (2019).

805 35 Lin, H.-H., Qraitem, M., Lian, Y., Taylor, S. R. & Farkas, M. E. Analyses of BMAL1 and PER2
806 Oscillations in a Model of Breast Cancer Progression Reveal Changes With Malignancy. *Integr*
807 *Cancer Ther* **18**, 1534735419836494-1534735419836494, doi:10.1177/1534735419836494
808 (2019).

809 36 Lellupitiyage Don, S. S. *et al.* Circadian oscillations persist in low malignancy breast cancer
810 cells. *Cell Cycle* **18**, 2447-2453, doi:10.1080/15384101.2019.1648957 (2019).

811 37 Baggs, J. E. *et al.* Network Features of the Mammalian Circadian Clock. *PLOS Biology* **7**,
812 e1000052, doi:10.1371/journal.pbio.1000052 (2009).

813 38 Gupta, G. K. *et al.* Perspectives on Triple-Negative Breast Cancer: Current Treatment
814 Strategies, Unmet Needs, and Potential Targets for Future Therapies. *Cancers (Basel)* **12**, 2392,
815 doi:10.3390/cancers12092392 (2020).

816 39 Fallahi-Sichani, M., Honarnejad, S., Heiser, L. M., Gray, J. W. & Sorger, P. K. Metrics other
817 than potency reveal systematic variation in responses to cancer drugs. *Nat Chem Biol* **9**, 708-
818 714, doi:10.1038/nchembio.1337 (2013).

40 Nagoshi, E. *et al.* Circadian gene expression in individual fibroblasts: cell-autonomous and self-sustained oscillators pass time to daughter cells. *Cell* **119**, 693-705, doi:10.1016/j.cell.2004.11.015 (2004).

41 Izumo, M., Johnson, C. H. & Yamazaki, S. Circadian gene expression in mammalian fibroblasts revealed by real-time luminescence reporting: Temperature compensation and damping. *Proceedings of the National Academy of Sciences* **100**, 16089-16094, doi:doi:10.1073/pnas.2536313100 (2003).

42 Balsalobre, A., Damiola, F. & Schibler, U. A Serum Shock Induces Circadian Gene Expression in Mammalian Tissue Culture Cells. *Cell* **93**, 929-937, doi:https://doi.org/10.1016/S0092-8674(00)81199-X (1998).

43 Bieler, J. *et al.* Robust synchronization of coupled circadian and cell cycle oscillators in single mammalian cells. *Mol Syst Biol* **10**, 739, doi:10.15252/msb.20145218 (2014).

44 Gérard, C. & Goldbeter, A. Entrainment of the Mammalian Cell Cycle by the Circadian Clock: Modeling Two Coupled Cellular Rhythms. *PLOS Computational Biology* **8**, e1002516, doi:10.1371/journal.pcbi.1002516 (2012).

45 Bernard, S., Čajavec Bernard, B., Lévi, F. & Herzel, H. Tumor Growth Rate Determines the Timing of Optimal Chronomodulated Treatment Schedules. *PLOS Computational Biology* **6**, e1000712, doi:10.1371/journal.pcbi.1000712 (2010).

46 Finger, A.-M. *et al.* Intercellular coupling between peripheral circadian oscillators by TGF-β signaling. *Science Advances* **7**, eabg5174, doi:doi:10.1126/sciadv.abg5174 (2021).

47 Balsalobre, A. *et al.* Resetting of Circadian Time in Peripheral Tissues by Glucocorticoid Signaling. *Science* **289**, 2344-2347, doi:10.1126/science.289.5488.2344 (2000).

48 version 9.11.0.1769968 (R2021b) (The MathWorks Inc., 2021).

49 Leise, T. L. & Harrington, M. E. Wavelet-based time series analysis of circadian rhythms. *J Biol Rhythms* **26**, 454-463 (2011).

50 Lee, G. R., Gommers, R., Waselewski, F., Wohlfahrt, K. & O'Leary, A. PyWavelets: A Python package for wavelet analysis. *Journal of Open Source Software* **4**.

51 Myung, J. *et al.* The choroid plexus is an important circadian clock component. *Nature Communications* **9**, 1062, doi:10.1038/s41467-018-03507-2 (2018).

52 Leise, T. L. Wavelet analysis of circadian and ultradian behavioral rhythms. *Journal of Circadian Rhythms*, doi:10.1186/1740-3391-11-5 (2013).

53 Barretina, J. *et al.* The Cancer Cell Line Encyclopedia enables predictive modelling of anticancer drug sensitivity. *Nature* **483**, 603-607, doi:10.1038/nature11003 (2012).

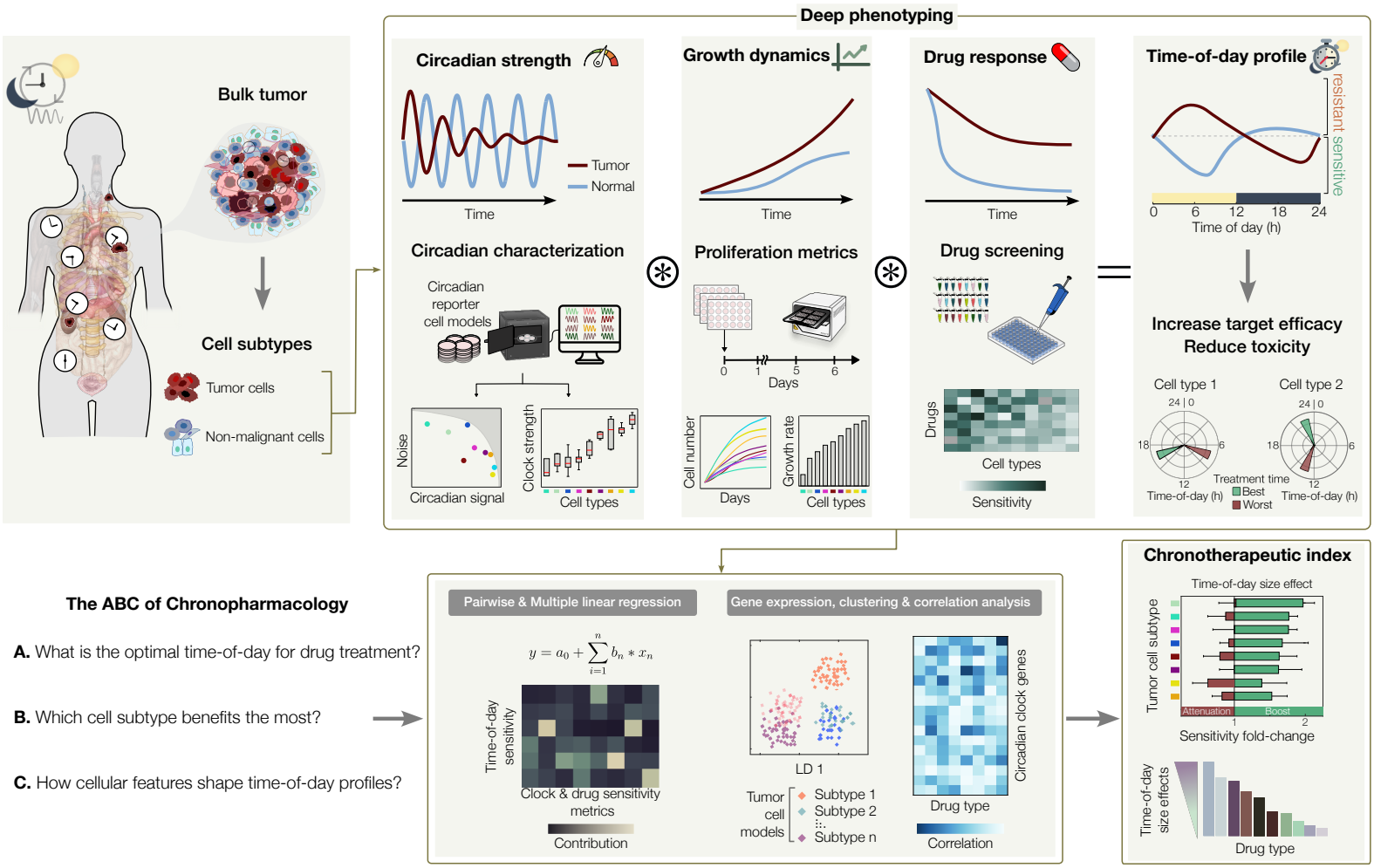

Fig. 1 | Framework for identifying optimal treatment times in cancer and healthy tissue models. Schematic overview of the experimental and computational framework to thoroughly characterize time-of-day drug responses in a variety of cell subtypes, such as cancer and non-malignant cell models. A combination of live recordings is implemented for the deep phenotyping of circadian strength, growth dynamics and drug responses that shape time-of-day profiles. Using a novel streamlined experimental approach, time-of-day sensitivity profiles are obtained in tumor and non-malignant cell models, providing best and worst timings for increased efficacy and reduced toxicity (*top panel*). A tandem computational pipeline integrates the deep phenotyping metrics as well as gene expression data of circadian clock genes to quantitatively address three fundamental questions in chronopharmacology (*bottom panel*). Combining multiple signatures, we define a chronotherapeutic index, ranking cellular models and drug agents by their size-effect gains from drug treatments aligned with the circadian clock (*bottom right panel*).

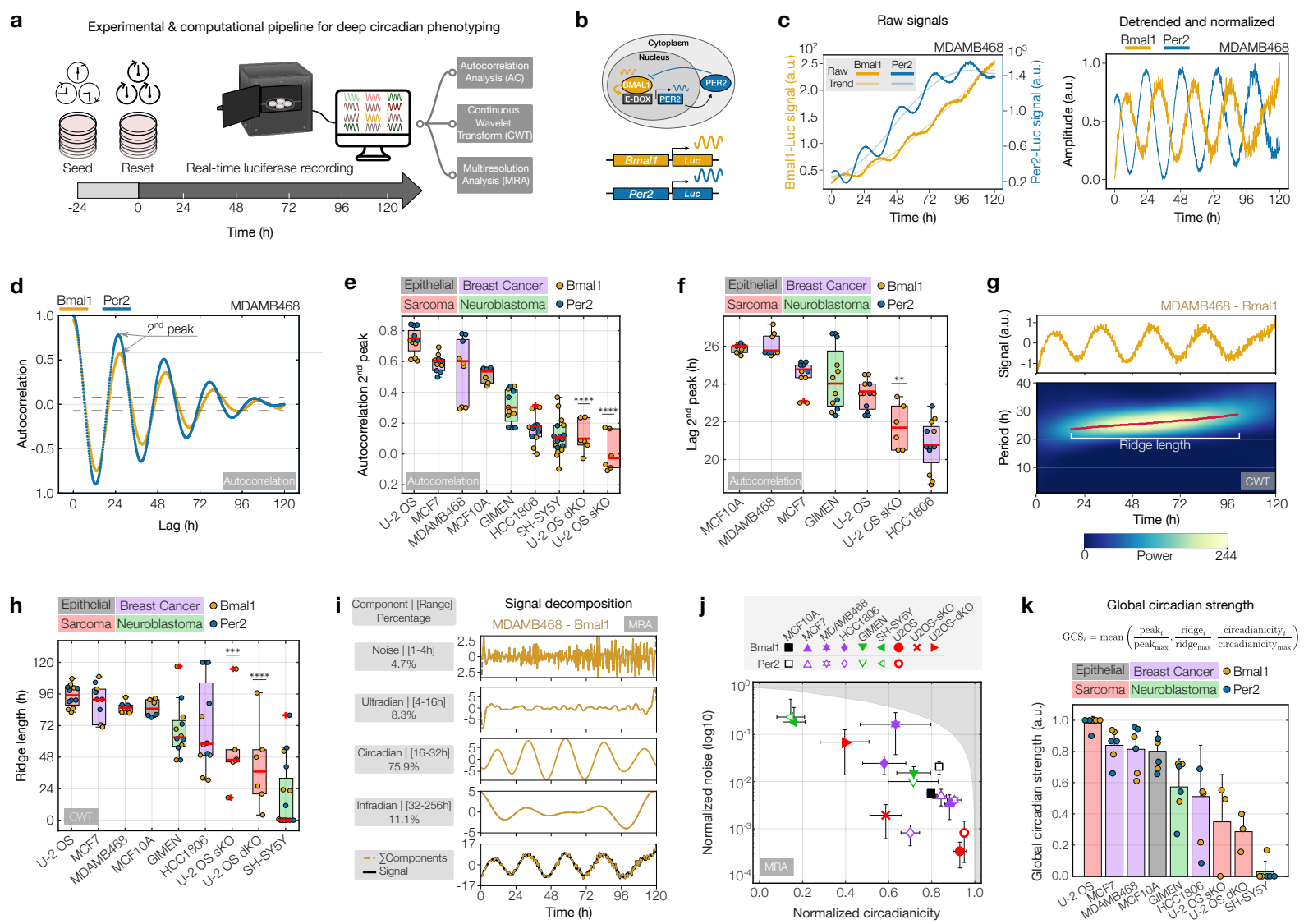

Fig. 2 | Determining circadian clock strength in cancer and healthy tissue cell models. a, Schematic of the experimental setup to detect circadian oscillations. **b,** Circadian feedback loops involving the core clock genes *Bmal1* and *Per2*, used here as circadian Luc-reporters. **c,** Raw (*left*) and processed (*right*) signals from MDAMB468-*Bmal1*/*Per2*-Luc cells. **d,** Autocorrelation (AC) of signals shown in **c**. Arrow indicates 2nd peak and corresponding abscissa (lag). Dashed lines=95.4% CI. **e,** Boxplot of AC values and **f,** corresponding lags at the 2nd peak of signals from various cell models. **g,** Detrended and amplitude-normalized signal (*top*) and corresponding wavelet power spectrum (*bottom*) obtained from continuous wavelet transform (CWT) showing time-resolved periods of signals from MDAMB468-*Bmal1*-Luc cells. Main oscillatory component (ridge) marked as red line. **h,** Boxplot of CWT ridge lengths of signals from the indicated cell models. Bottom and top edges of the boxes in **e**, **f**, and **h** indicate the 25th and 75th percentiles, respectively. Red horizontal lines denote the data's median and red crosses outliers. *n*=6–17 technical replicates, collected from two Luc-reporters. **i,** Multiresolution analysis (MRA) of detrended MDAMB468-*Bmal1*-Luc signals. %=fraction of respective component to total signal. **j,** Scatterplot of normalized noise versus circadianicity of signals from the indicated cell models, determined by MRA. Shaded area covers unattainable range. Data represents the mean ± s.d. *n*=3–9 technical replicates. **k,** Bar diagram ranking cell models by their global circadian strength integrating parameters obtained from AC (peak), CWT (ridge) and MRA (circadianicity). Data represents the mean ± s.d. For representation purposes only the positive s.d. is shown. *n*=3–6. Color coding of data shown in **b–i** and **k** according to the corresponding Luc-reporter for *Bmal1* (yellow) and *Per2* (blue). Color coding of different cell models in **e**, **f**, and **h–k** according to the tissue of origin. A two-sample *t*-test assuming equal variances was used to evaluate statistical significance, where **, *** and ****, indicate *p*-values<0.01, 0.001, and 0.0001, respectively.

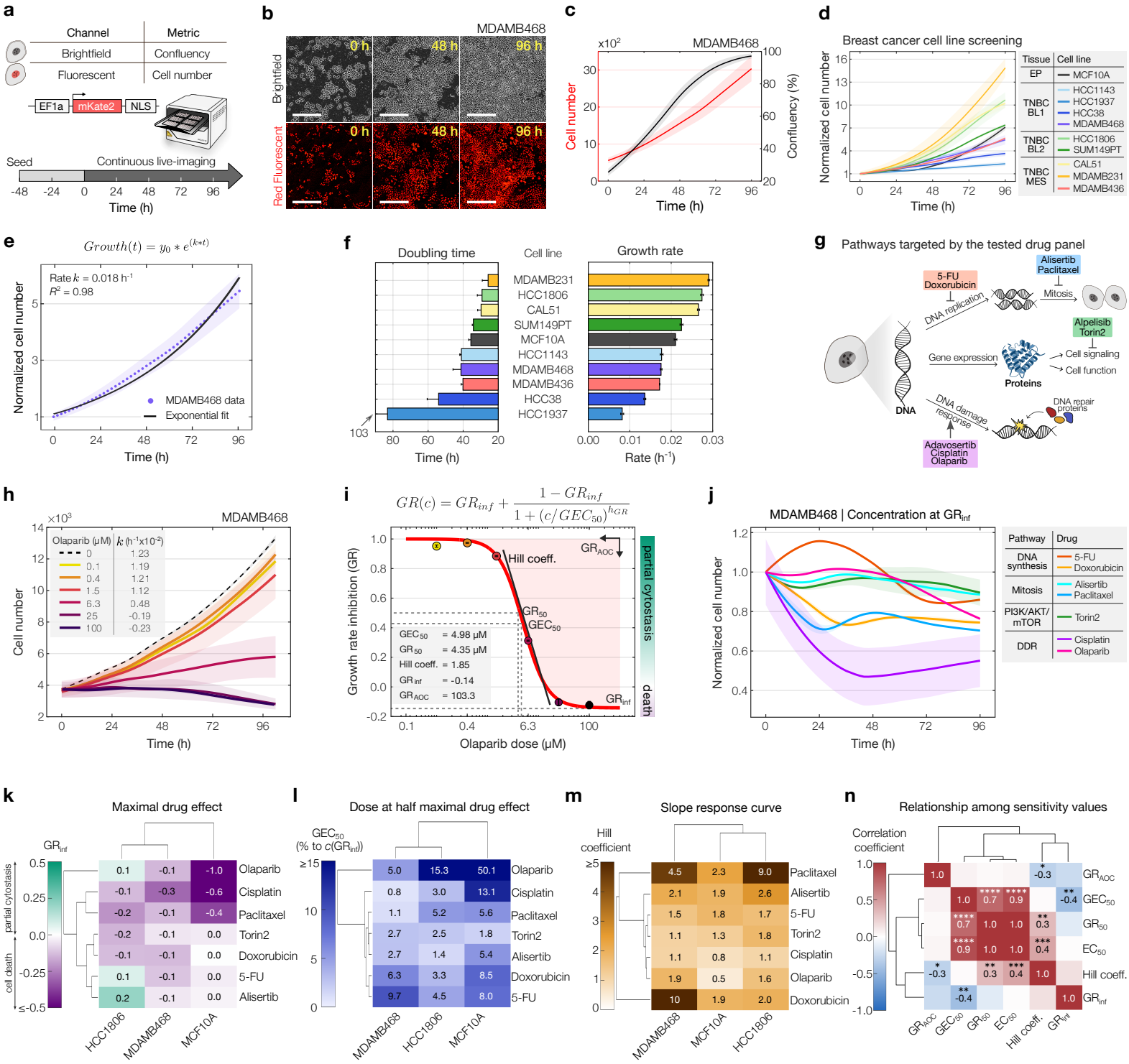

Fig. 3 | Unravelling growth and drug response dynamics through long-term live-cell imaging. a, Schematic of the setup for capturing cell growth using fluorescent nuclear reporters. **b,** Bi-daily snapshots of MDAMB468 cell growth in the brightfield (*top*) and red fluorescent channel (*bottom*). Ruler = 400 μM. **c,** MDAMB468 confluency (*black line*) and cell numbers (*red line*) over time. **d,** Normalized growth curves of the indicated cell models. **e,** Exponential fit for MDAMB468 growth curves, yielding the growth rate (*k*), and fit accuracy (R^2). **f,** Bar diagrams ranking cell models by doubling times and growth rates. Data in **c–f** represents the mean ± s.e.m. from 9 snapshots. *k*-value errors reflect the 95% CI. For clarity in **f**, one-sided error bars are shown, with the arrow indicating the top range of the respective error bar. **g,** Schematic of the pathways targeted by the drugs used in this study. **h,** Cell numbers and corresponding *k*-values of MDAMB468 cells treated with varying olaparib doses (color-coded) or solvent (dashed line). Data represents the mean ± s.d. of two plates. **i,** Dose-response curve of *GR* values corresponding to **h**, highlighting various drug sensitivity metrics. Error bars = 95% CI. **j,** Normalized numbers of MDAMB468 cells treated with the GR_{inf} dose of the indicated drugs. Data represents the mean ± s.d. of two plates, or ± s.e.m of 9 snapshots (cisplatin). **k–m,** Hierarchical clustering of drug sensitivity parameters across cell-drug combinations. GEC_{50} values in **l** are shown relative to the GR_{inf} dose. **n,** Pearson's linear correlation coefficients of sensitivity parameters shown in **k–m** and additional cell-drug combinations (see Supplementary Table 1; *n*=49–50). A two-sample *t*-test assuming equal variances was used to evaluate statistical significance; *, **, *** and ****, indicate *p*-values<0.05, 0.01, 0.001, and 0.0001, respectively. Denoted are significant correlation coefficients. Data in **k–n** based on the mean of two plates or 9 snapshots (cisplatin).

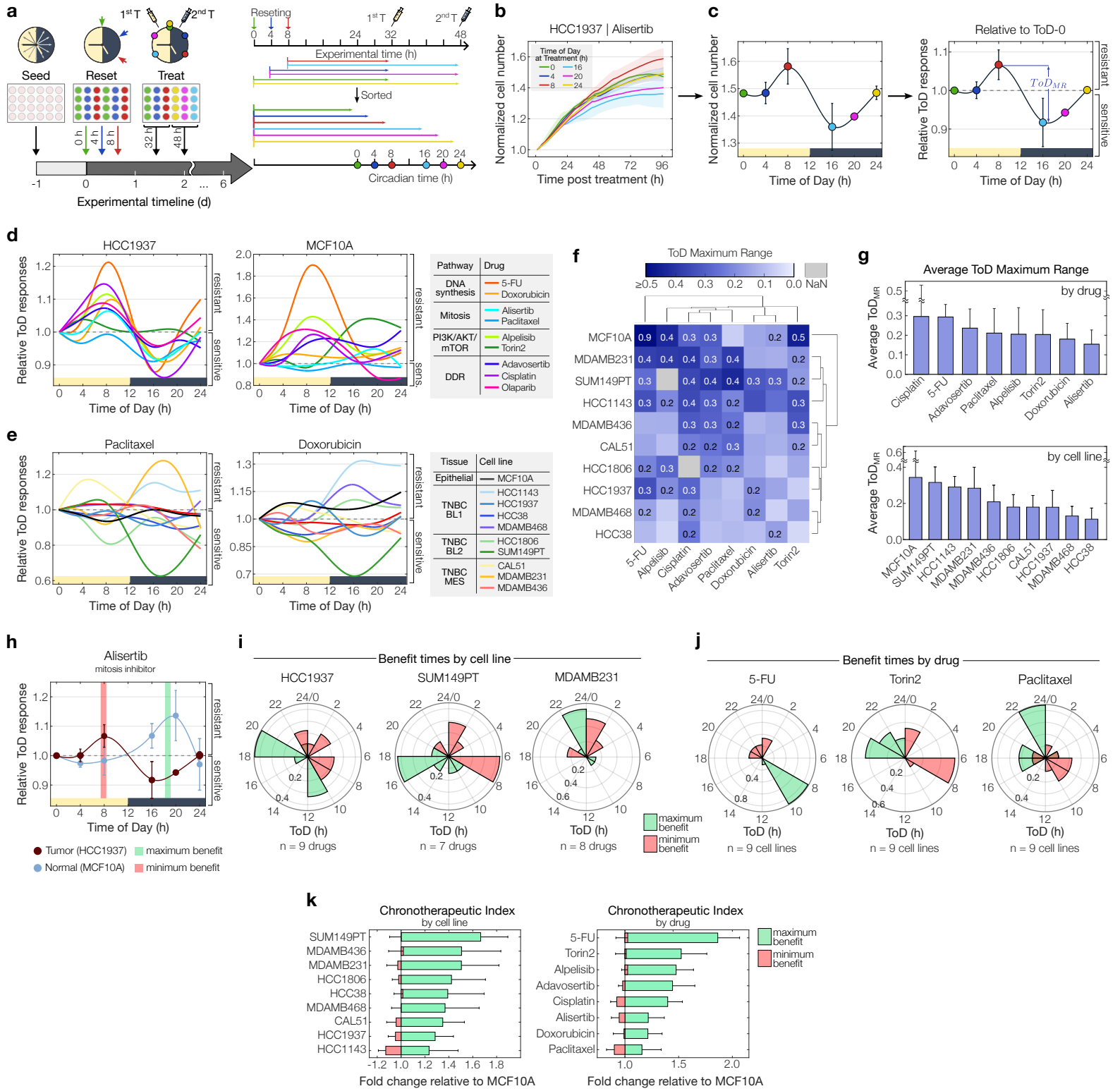

Fig. 4 | Time-of-day drug sensitivity is drug and tissue model dependent. a, Schematic of the experimental setup to screen for time-of-day (ToD) responses. Three clock-resetting steps are performed in 4-h intervals. Drugs are administered 32 or 48 h post-initial reset, resulting in six circadian times (0, 4, 8, 16, 20 and 24 h). Growth is monitored by long-term live-cell imaging. Timelines on the right depict experimental (*top*) and relative circadian times (*bottom*), color-coded by each ToD tested. **b,** Cell counts of HCC1937 treated with alisertib at different times of the day. Normalization to respective time of treatment. **c,** Cell numbers 4 days post-treatment versus treatment times, corresponding to **b** (*left*). ToD response curve (ToD-RC) depicting relative responses to ToD 0 h. Blue arrows mark the maximum ToD response range (ToD_{MR}). **d,** ToD-RCs for HCC1937 or MCF10A cells treated with different drugs (color-coded). **e,** ToD-RCs for 10 cell models treated with paclitaxel or doxorubicin. Color coding of cell models according to tissue of origin. **f,** Hierarchical clustering of ToD_{MR} values across drug-cell combinations. Values above 0.2 are shown. Data clustering with the UPGMA method and euclidian distance. **g,** Bar diagrams ranking ToD_{MR} values per drug and cell model. **h,** ToD-RCs for alisertib-treated HCC1937 tumor and MCF10A non-tumor cells overlaid, yielding maximum and minimum benefit times. Data shown in **b–h** represents mean (± s.d.) of two plates. **i,** Polar histograms for benefit times across cell models (*n*=7–9 drugs) and j, drugs (*n*=9 cell models). **k,** Butterfly charts depicting fold changes relative to MCF10A at benefit times, averaged per cancer cell model (*left*) and drug (*right*). Color-coding of maximum and minimum benefit times shown in **h–k** in green and red, respectively. Data shown in **g** and **k** represents mean ± s.d. of tested cell models per drug and vice versa (*see* **f**). For clarity, one-sided error bars are shown.

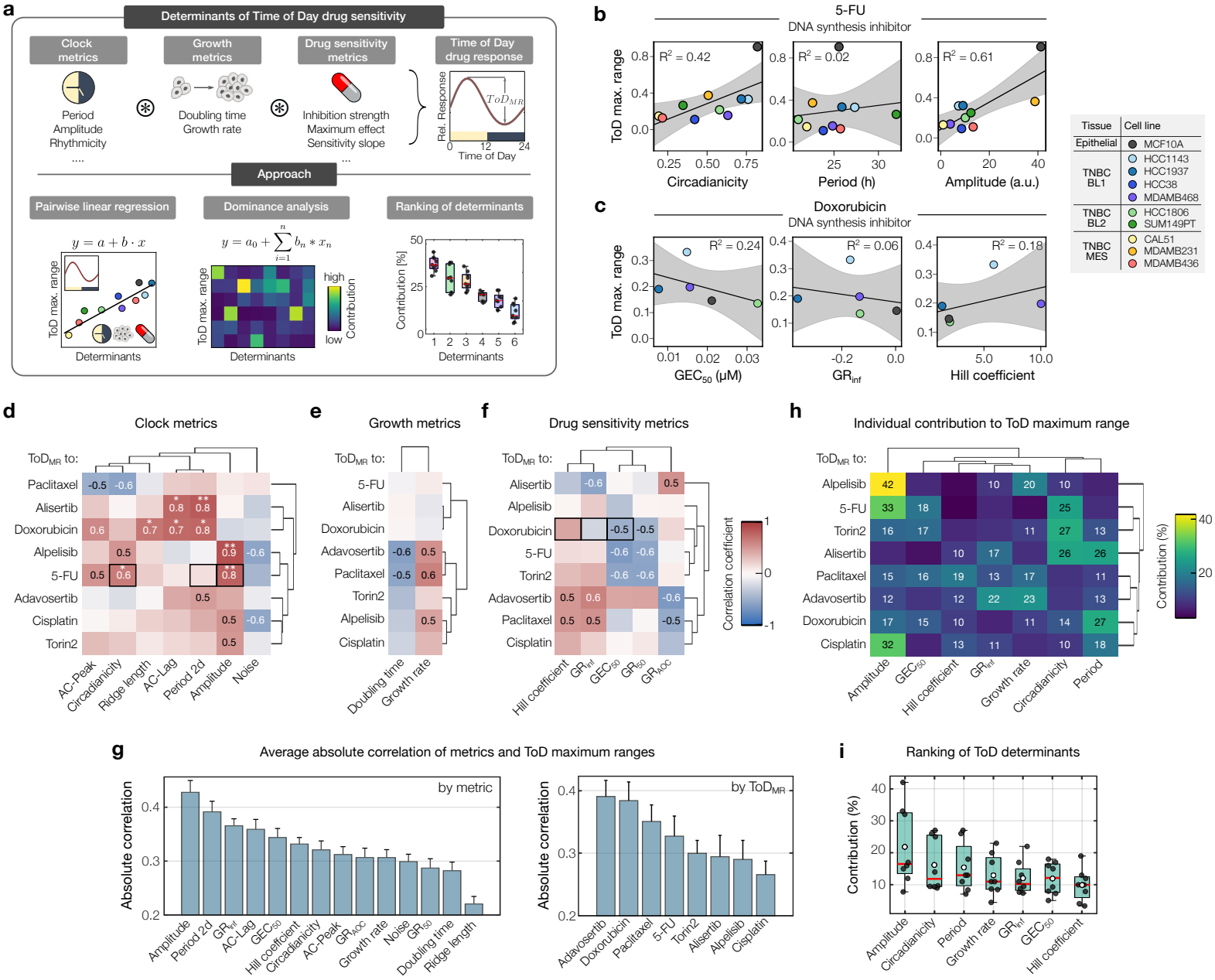

Fig. 5 | Clock and drug sensitivity metrics shape ToD curves. a, Computational approach to investigate how circadian rhythms, cell growth dynamics, and drug sensitivity factors influence the time-of-day (ToD) drug efficacy. **b,** and **c,** Example of linear correlations between ToD_{MR} and circadian (**b**) or drug sensitivity parameters (**c**), for 5-FU (*n*=10 cell models) and cisplatin (*n*=5 cell models), respectively. Color coding of cell models according to tissue of origin. Grey-shaded area=95% CI. Model accuracy indicated by R^2-values. **d–f**, Hierarchical clustering of correlation coefficients (*r*) between ToD_{MR} values of different drugs (*rows*) and the respective metric (*columns*) for clock strength (**d**, *n*=10 cell models), growth (**e**, *n*=10 cell models) or drug sensitivity (**f**, *n*=5 cell models). *r*-values ≥ 0.5 and ≤ -0.5 are shown. Black boxes indicate examples shown in **b** and **c**. A two-sample *t*-test assuming equal variances was used to evaluate statistical significance; *, and **, indicate *p*-values <0.05, and 0.01, respectively. *Note*: for alpelisib in **d–f** sample size=(*n*-1); for cisplatin in **d** and **e**, *n*=9 and in **f**, *n*=9. **g,** Bar diagrams ranking the absolute correlation between ToD_{MR} values and each metric depicted in **d–f**, ranked by metric (*n*=8 drugs) or by drug (*n*=14 metrics). Data represents the mean ± s.e.m. For clarity, one-sided error bars are shown. **h,** Hierarchical clustering of the dominance analysis matrix showing the individual contribution of circadian clock, growth and drug sensitivity parameters (*columns*) in predicting drug dependent ToD_{MR} values (*rows*). Colors indicate the percentage contribution, as detailed in the color bar. See key for **d–f** for sample sizes (*n*). **i,** Boxplot of overall contribution of cellular metrics to predict ToD_{MR} values, corresponding to **h**. Black data points indicate the individual result from each drug (*n*=8 drugs). Red horizontal lines denote the median, white circles denote the mean. Bottom and top edges of the boxes indicate the 25th and 75th percentiles, respectively.

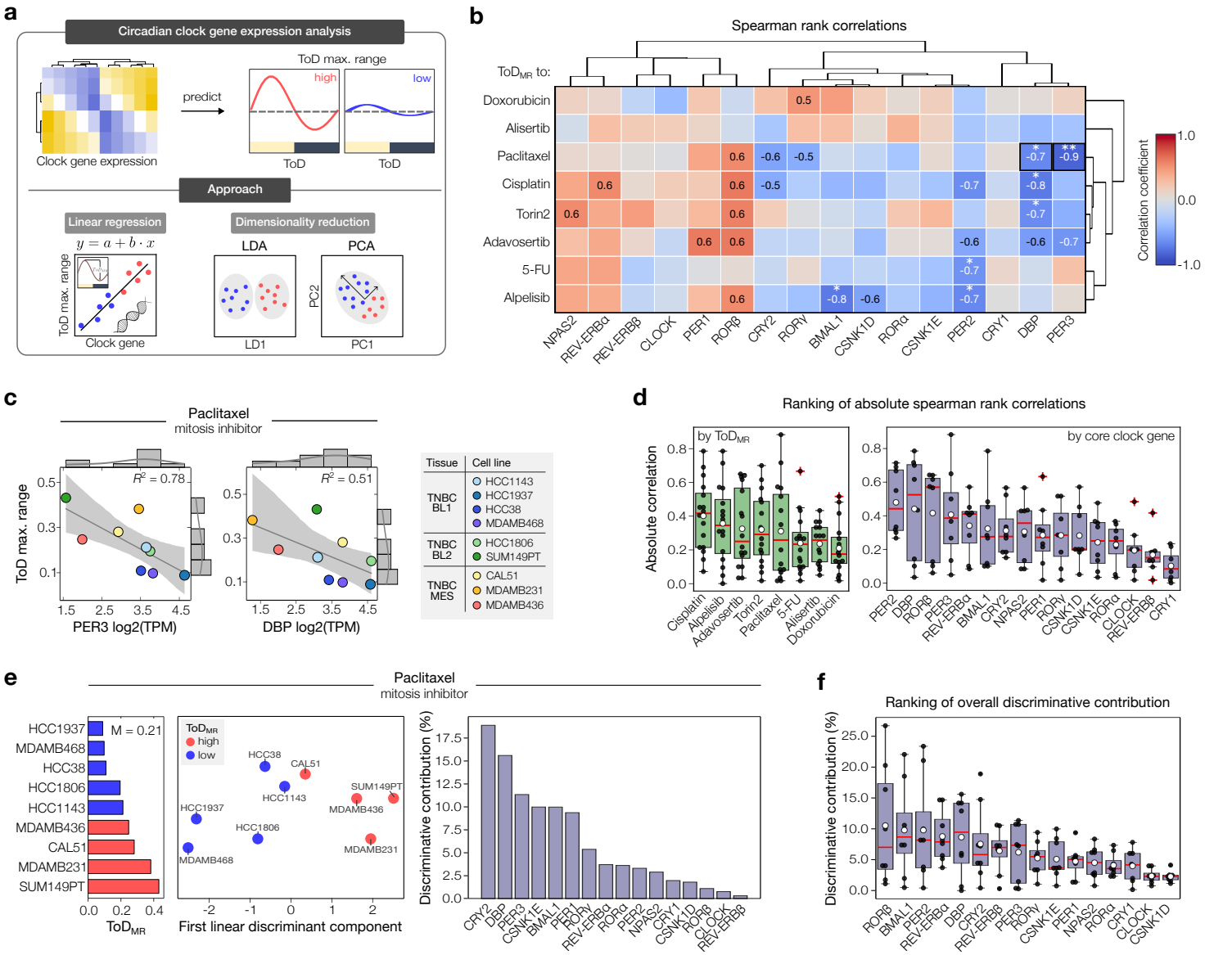

Fig. 6 | Gene expression analysis unveils diverse roles of circadian genes in determining time-of-day patterns. a, Approach to identify the role of core clock genes that determine the strength of time-of-day (ToD) drug sensitivity. **b,** Hierarchical clustering of spearman rank correlation coefficients between drug-dependent ToD$_{MR}$ values (*rows*) and core clock genes (*columns*). Black boxes indicate examples shown in **c**. Statistical significance of the correlations were calculated, where *, and **, indicate *p*-values<0.05, and 0.01, respectively. Cisplatin and alpelisib: *n*=8 cell lines, else *n*=9 cell lines. **c,** Example of linear correlation analysis between paclitaxel ToD$_{MR}$ values and *Per3* or *Dbp* expression levels measured as log2(TPM). Color-coded data points indicate different tumor cell models. Grey-shaded area=95% CI. Model accuracy indicated by R^2-values. Top and lateral histograms indicate the count of samples along the range of gene expression, and ToD$_{MR}$ values, respectively. The grey continuous line indicates the normal distribution fit of the samples. *n*=9 cell lines. **d,** Boxplot showing the mean-based ranking of absolute spearman rank correlation values between circadian clock gene expression levels and ToD$_{MR}$ values, categorized by drug (*n*=16 circadian clock genes) or by circadian clock gene (*n*=8 drugs). **e,** Linear discriminant analysis (LDA) on median-based binarized ToD$_{MR}$ values for paclitaxel. Cell models with ToD$_{MR}$ values below or above the median (M) are colored in blue and red, respectively (*middle and left panel*). The contribution to the obtained discriminative information is shown in percentage for each of the circadian clock genes (*right panel*). **f,** Boxplot showing the mean-based ranking of overall discriminative contributions of each circadian clock gene across all tested drugs. *n*=8 drugs. Bottom and top edges of the boxes shown in **d** and **f** indicate the 25th and 75th percentiles, respectively. Red horizontal lines denote the median, white circles denote the mean, and red crosses indicate outliers.

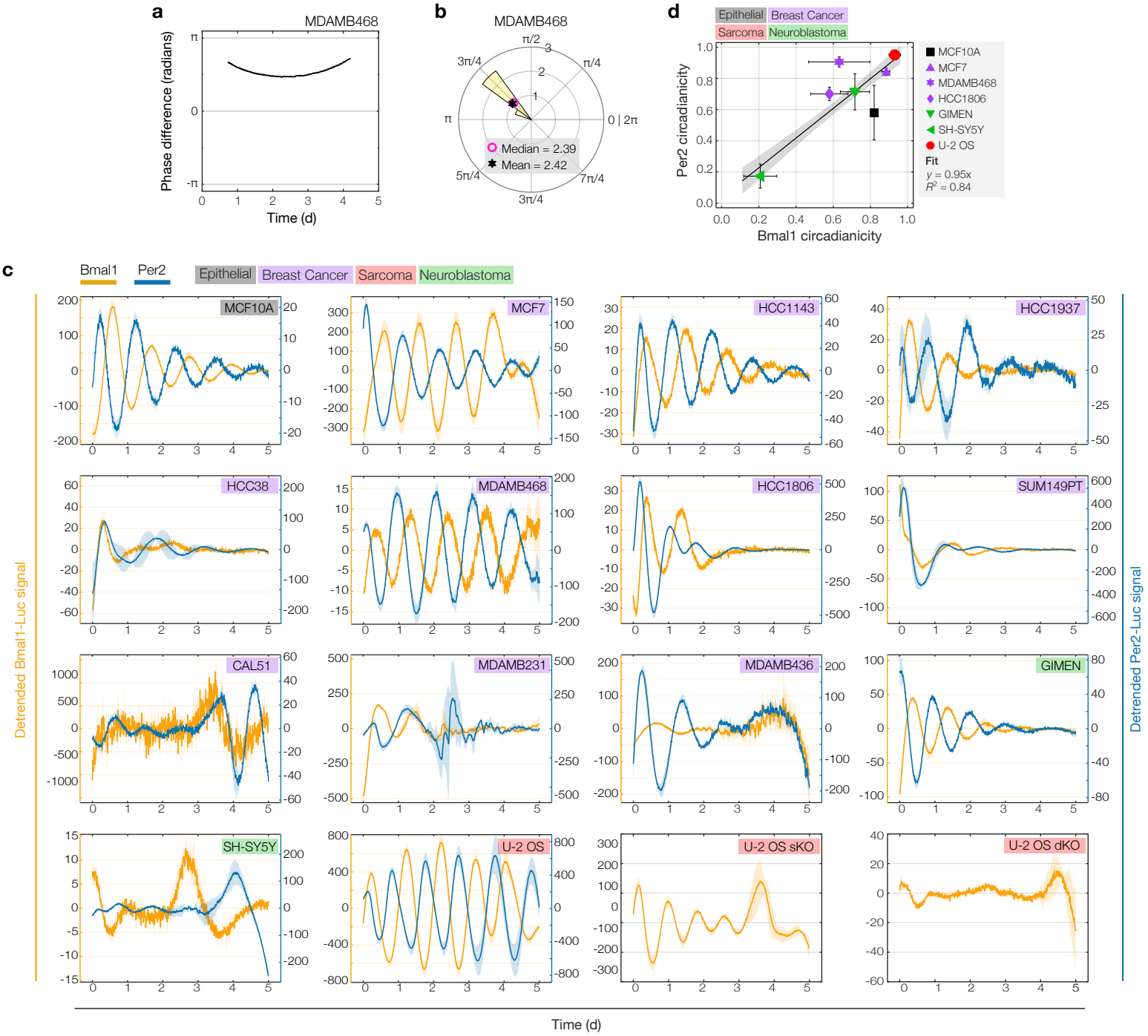

Supplementary Fig. 1. a, Example of absolute phase difference evolution analysis between *Bmal1*- and *Per2*-Luc signals here shown for single samples of MDAMB468 cells. **b,** Polar histogram depicting the phase difference between *Bmal1* and *Per2* signals in MDAMB468 cells over time. 2π denotes one full circadian cycle. Median and mean phase difference are indicated as pink circle and black star, respectively. **c,** Detrended *Bmal1*- (*yellow*) and *Per2*-Luc (*blue*) signals of all cell lines used in this study. **d,** Linear regression analysis of the MRA circadian component ('circadianicity') of *Bmal1*- versus *Per2*-Luc signals. Markers indicate different cell models. Data represents the mean ± s.d. (*n*=3–9 technical replicates). Grey-shaded area=95% CI. Model accuracy indicated by R^2-values. Color coding of cell models in **c** and **d** according to their tissue of origin. Data depicted in **c** and **d** represents the mean ± s.d. of 3–9 technical replicates.

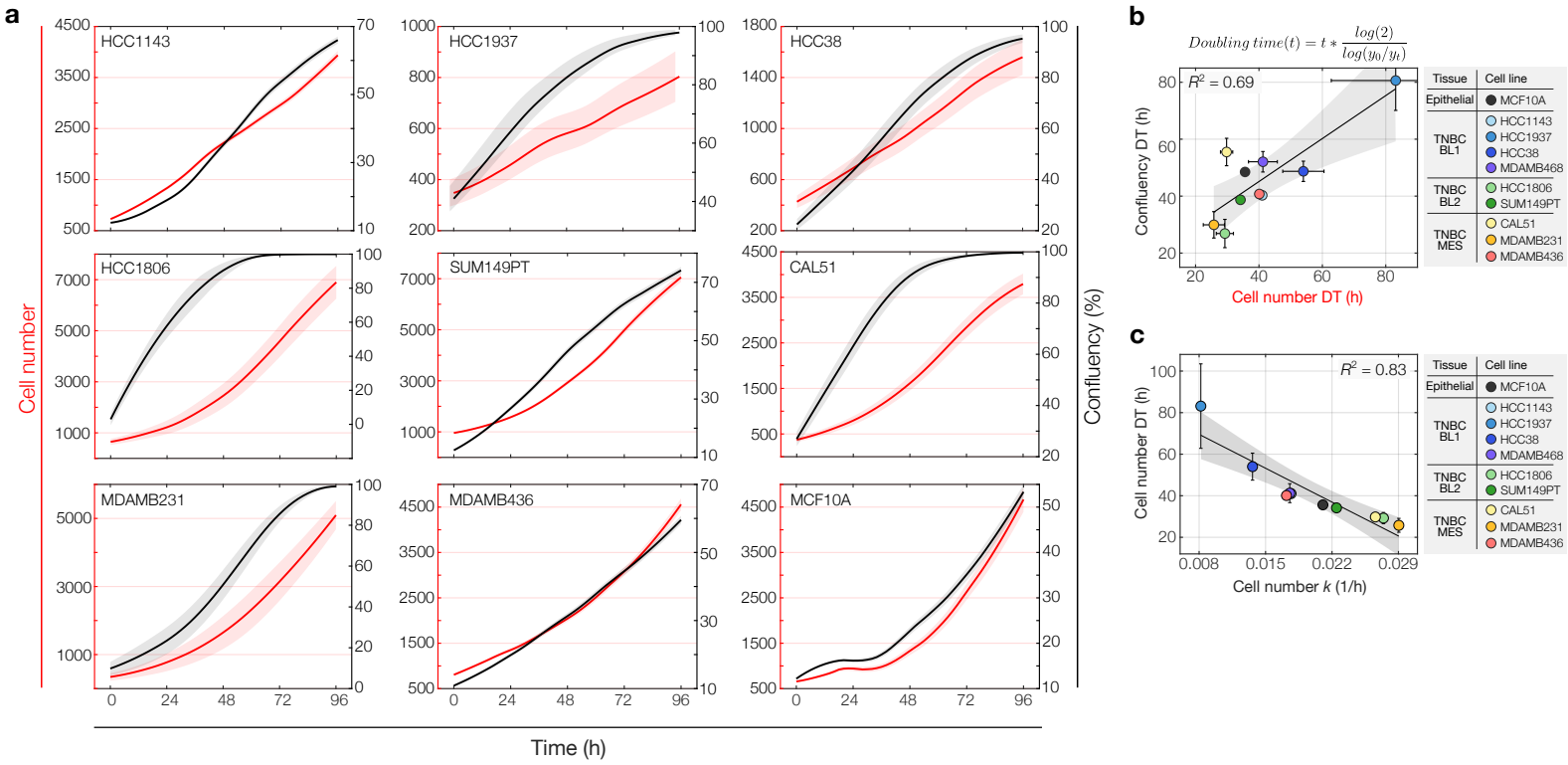

Supplementary Fig. 2. a, Growth curves of the indicated cell lines monitored by live-cell imaging for 4 days quantified by cell numbers (*red line*) or confluency (*black line*). Data represents the mean ± s.e.m. of 9 images. **b,** Linear regression analysis of doubling times (DT's) calculated from confluency versus cell numbers. **c,** Linear regression analysis of the doubling time and growth rate (*k*) calculated from cell numbers of various cell lines.
Color coding of cell models in **b** and **c** according to their tissue of origin. Data shown in **b** and **c** represents the mean ± s.d. (DT's), or ± CI of the exponential fit (*k*-values). Grey-shaded area=95% CI. Model accuracy indicated by R^2-values.

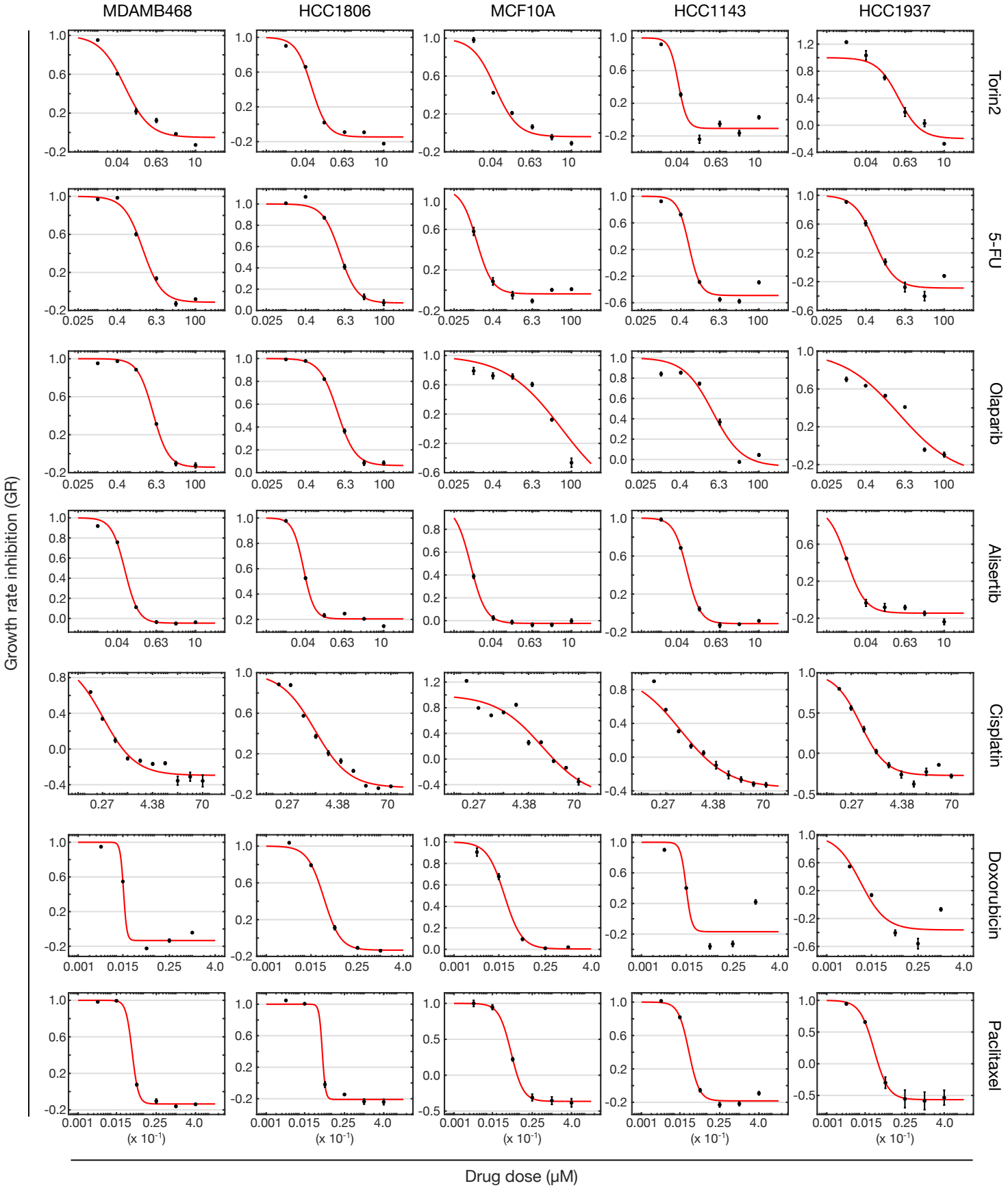

Supplementary Fig. 3. Dose-response curves of *GR* values for the specified cell models and drugs. The data is based on the mean of two plates or 9 images (cisplatin), assayed by live-cell imaging for 4 days. Error bars indicate the 95% CI of the exponential fit.

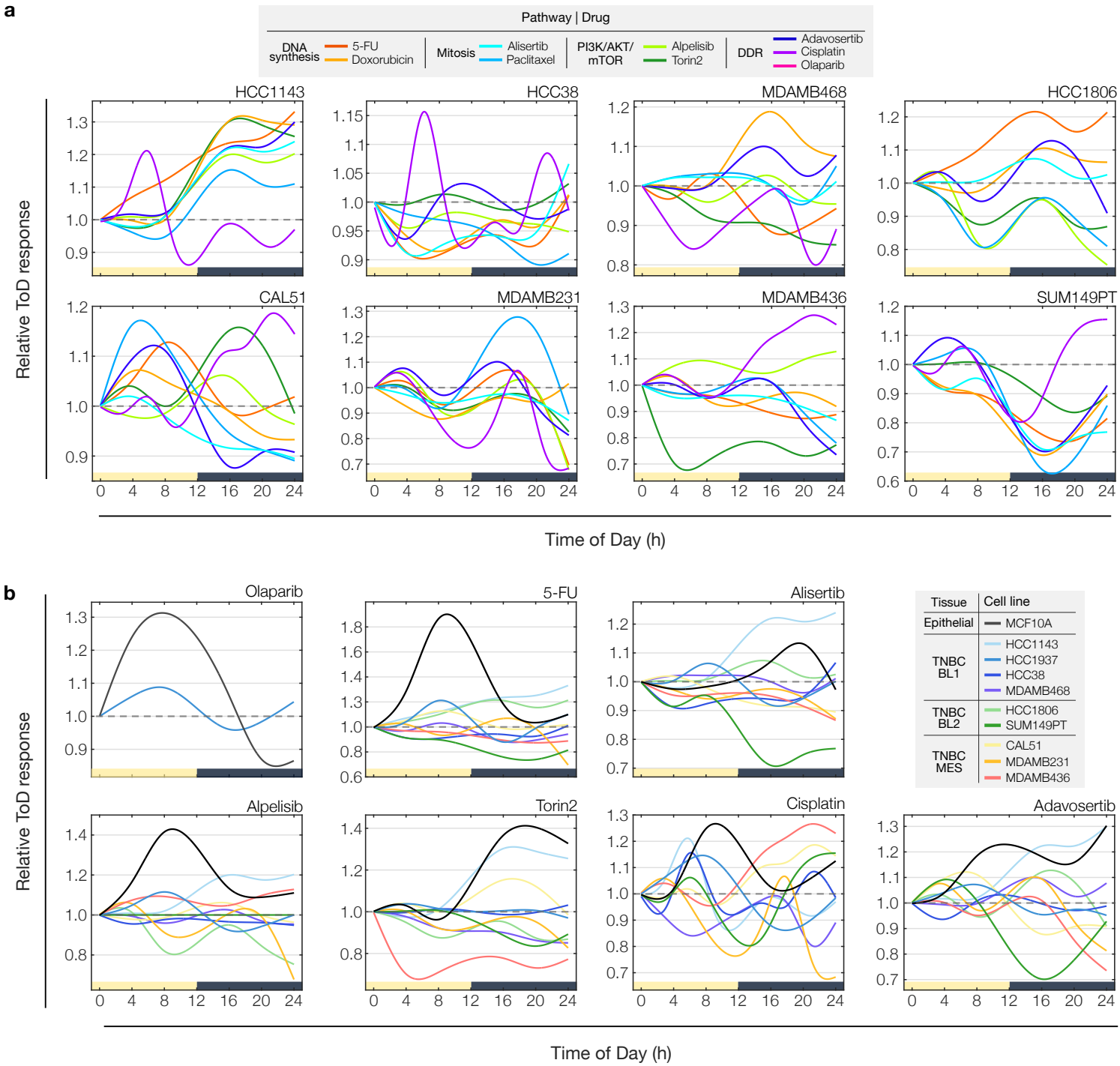

Supplementary Fig. 4. a, Overlay of ToD response curves (ToD-RCs) for individual cell models treated with different drugs (color-coded). **b,** Overlay of ToD-RCs for multiple cell models, grouped by the administered drugs. Cell line models are color-coded. Data in **a** and **b** represents the mean for each drug-cell combination tested on two plates or 9 images (cisplatin).

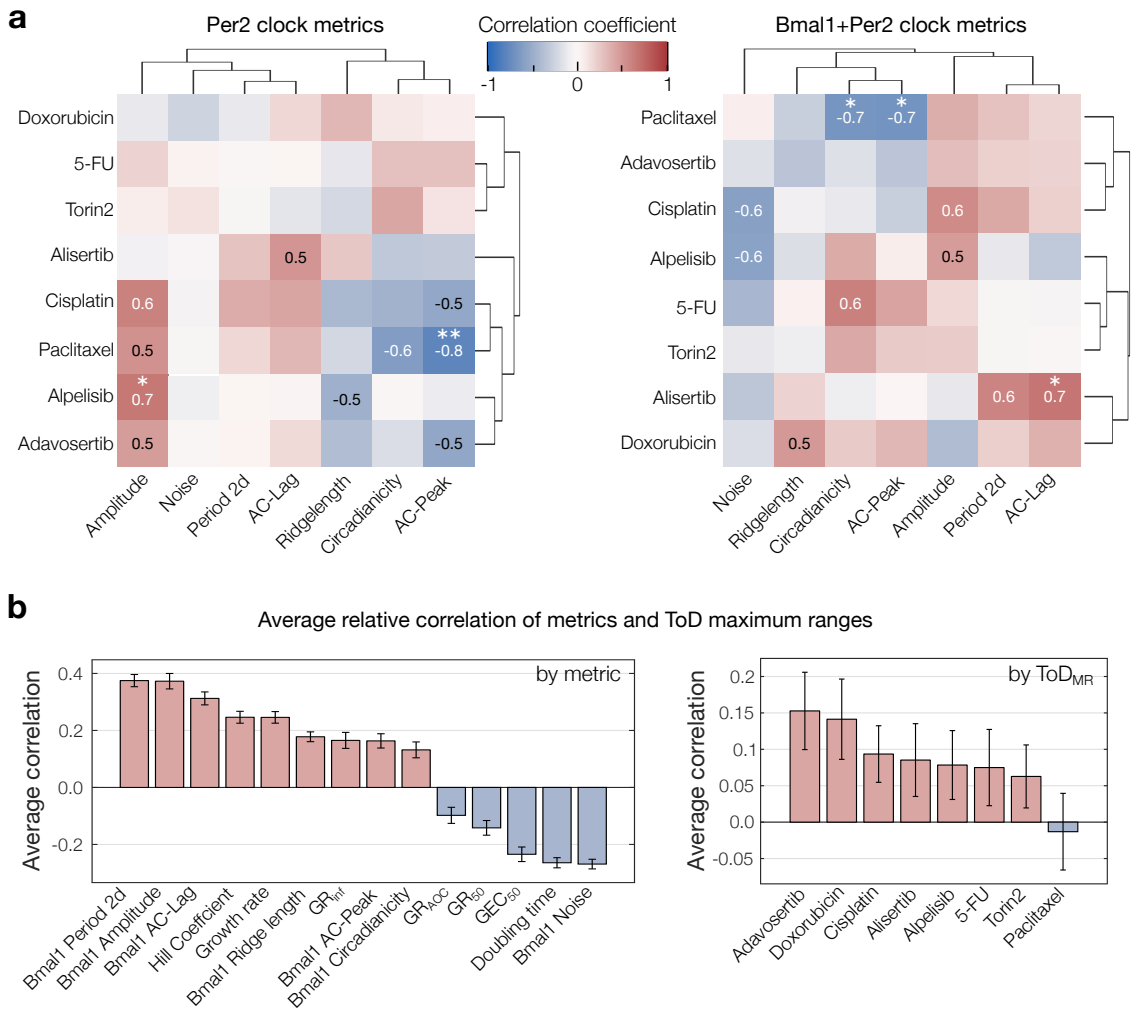

Supplementary Fig. 5. a, Hierarchical clustering of correlation coefficients between ToD_{MR} values for different drugs (*rows*) and clock strength metrics (*columns*) obtained from the *Per2*-reporter (*left*) or calculated as a mean from the *Bmal1*- and *Per2*-reporter (*right*). A two-sample *t*-test assuming equal variances was used to evaluate statistical significance; *, and **, indicate *p*-values <0.05, and 0.01, respectively. n=10 or 9 (cisplatin and alpelisib) cell models. **b,** Bar plots ranking relative overall correlation between ToD_{MR} values and individual cellular metrics (depicted in **Fig. 5d–f**), averaged by metric (*left*, n=8 drugs) or by drug (*right*, n=14 metrics). Positive and negative correlation values are color-coded in light red and blue, respectively. Data represents the mean ± s.e.m.

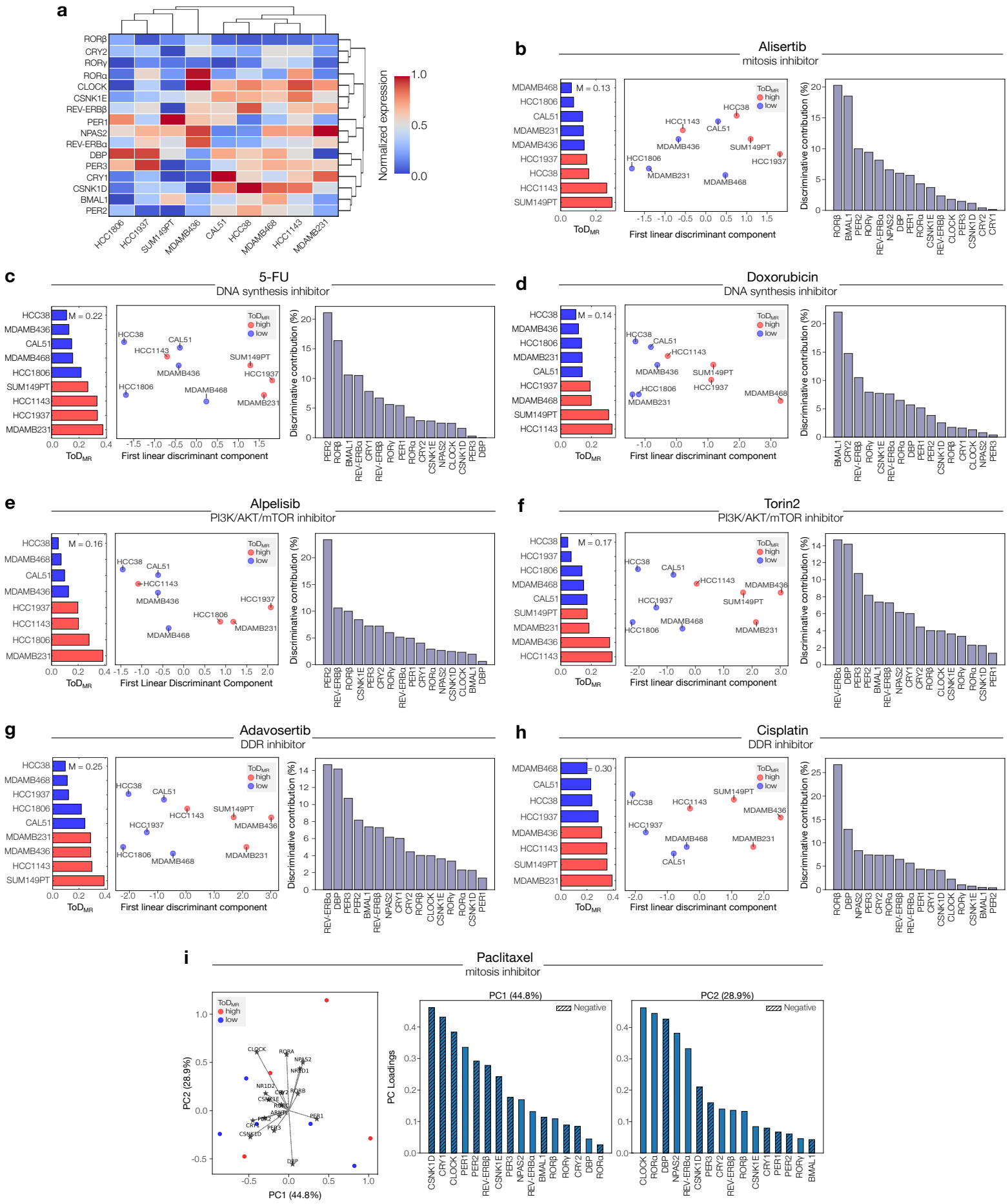

Supplementary Fig. 6. a, Gene expression clustermap of the selected list of core clock genes (*rows*) for the different cell models (*columns*) used in this work. **b-h,** Linear discriminant analysis on median-based binarized ToD_{MR} values for the indicated drugs. ToD_{MR} values below or above the median (M) are color-coded as blue and red, respectively (*middle and left panel of each subfigure*). The contribution to the obtained discriminative information is shown in percentage for each of the circadian clock genes (*right panel of each subfigure*). **i,** Principal component analysis (PCA) biplot of the first two principal component scores on ToD sensitivity groups related to paclitaxel. The principal components for the circadian clock genes are super-imposed with the PCA biplot scores at the similar scale that reflects the contribution of the variables in determination of ToD sensitivity groups (color-coded, *left panel*). The variance (PC loadings) explained by each component is expressed in percentage (*middle and right panel*).

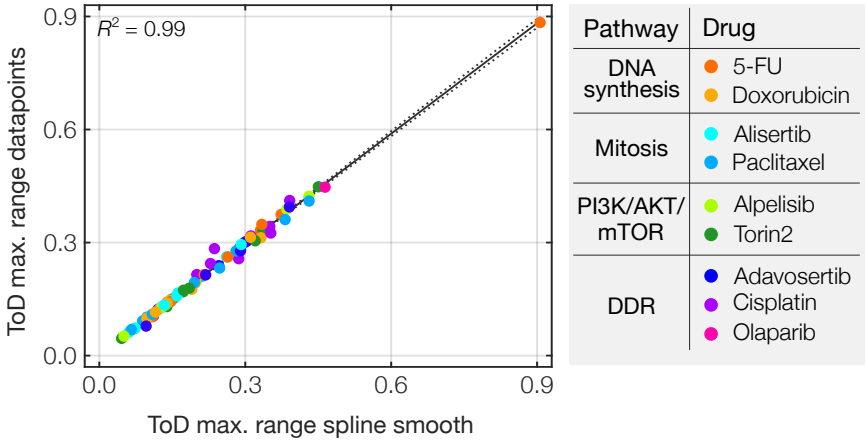

Supplementary Fig. 7. Linear regression analysis of the maximum range in ToD responses (ToD_{MR}) determined from discrete measured data points or from continuous spline smoothed curves. Drugs are color-coded. Dotted lines=95% CI. Model accuracy indicated by R^2-values. Data represents the mean ± s.d. of 4-day live-cell imaging recordings for each drug tested on two plates or 9 images (cisplatin). *n*=80 drug-cell combinations.